# Palaeoproterozoic Orogenic Gold Style Mineralization at the Southwestern Archaean Tanzanian Cratonic Margin, Lupa Goldfield, SW Tanzania: Implications from U-Pb Titanite Geochronology

C.J.M. Lawley[1,2*], D. Selby[1], D. Condon[3] and J. Imber[1]

[1]Department of Earth Sciences, Durham University, Science Labs, Durham, DH1 3LE, UK
[2]Natural Resources Canada, Geological Survey of Canada, Ottawa, Ontario, K1A 0E8, Canada
[3]Natural Environment Research Council Isotope Geosciences Laboratory, British Geological Survey, Keyworth, Nottingham, NG12 5GG, UK

*corresponding author: e-mail: clawley@NRCan.gc.ca; Tel: 1 (613) 996-23593

**Abstract:** The Lupa Goldfield, situated at the southwestern Tanzanian cratonic margin, comprises a network of auriferous quartz veins and greenschist facies mylonitic shear zones cutting a suite of Archaean-Palaeoproterozoic granitic-gabbroic intrusions. The existing geochronological database points to a protracted, but episodic 1.96−1.88 Ga magmatic history that is broadly coincident with the 2.1–1.8 Ga Ubendian Orogeny. Molybdenite, pyrite and chalcopyrite samples from mineralized quartz veins and mylonitic shear zones yield Re-Os model ages that range from 1.95–1.88 Ga, whereas ca. 1.88 Ga pyrite with gold bearing inclusions and sampled from the host mylonitic shear zone suggest that gold occurred relatively late in this hydrothermal history. The ca. 1.88 Ga gold event is recorded at all five of the studied prospects, whereas the relationship between gold and the disparately older 1.95 and 1.94 Ga Re-Os molybdenite ages is unclear. New U-Pb metamorphic titanite dating of a foliated Archaean granite sample (ca. 2.76 Ga) suggests that the onset of ductile deformation within the Lupa Goldfield occurred at ca. 1.92 Ga, and some ca. 40 Myr prior to auriferous and brittle-ductile mylonitic shear zones at ca. 1.88 Ga. Early ductile deformation is not associated with gold mineralization, but the ductile deformation fabrics and, in particular the development of rheologically weak chloritic folia, may have acted as zones of pre-existing weakness that localized strain and influenced the geometry of later auriferous mylonitic shear zones. The large age difference between U-Pb zircon and titanite ages for the Archaean granite sample is in contrast to new U-Pb titanite ages for the Saza Granodiorite (1930 ± 3 Ma), which are only slightly outside of analytical uncertainty at the 2σ level with a previously reported U-Pb zircon

age for the same sample (1935 ± 1 Ma). These new age results, together with previously reported U-Pb and Re-Os ages, highlight the protracted magmatic, hydrothermal and structural evolution of the Lupa Goldfield (1.96–1.88 Ga). They are also consistent with other palaeo-convergent margins where orogenic gold systems genesis occurs relatively late in the orogen's tectono-thermal history.

Keywords: Lupa Goldfield, Paleoproterozoic, Orogenic Gold, Tanzania, Ubendian Belt

## 1.0 Introduction

### *1.1 Tanzanian gold deposits*

Tanzania represents the fourth largest gold producer in Africa and is the subject of renewed mineral exploration interest since the introduction of reformed mining legislation in the late 1990s (Roe and Essex, 2009; Yager, 2010; Brown et al., 2013). The vast majority of gold production and mineral exploration are concentrated in northern Tanzania and the Lake Victoria Goldfield where world-class deposits (i.e., deposits with ≥ 3.0 Moz of contained gold in proven and probable reserves) such as Geita (12.3 Moz; AngloGold Ashanti Annual Report, 2012) and Bulyanhulu (8.0 Moz; Barrick Annual report, 2012) are located (Fig. 1). Two other operating mines are also located in the Lake Victoria Goldfields [North Mara, 2.2 Moz (Barrick Annual report, 2012); Buzwagi, 2.0 Moz (Barrick Annual Report, 2012)] in addition to past producing mines (e.g., Golden Pride, Tulawaka) and numerous smaller-scale artisanal mining operations (Fig. 1). These deposits are hosted by Neoarchaean greenschist-amphibolite facies granite-greenstone belts and lesser sedimentary successions comprising the Tanzanian Craton and are typical of similarly-aged orogenic gold deposits worldwide (e.g., Goldfarb et al., 2001).

The Lake Victoria Goldfield represents merely one example of Tanzania's gold endowed regions (Fig. 1). Metamorphic belts contiguous with the Tanzanian Craton host a variety of lesser known goldfields (e.g., Lupa, Mpanda, Mbinga and Niassa) that have attracted comparatively less modern gold exploration. The geologic settings of these goldfields also remain poorly understood despite their historic importance during Tanzania's colonial period and on-going artisanal mining activity (van Straaten, 1984; Kuehn et al., 1990). Recent geochronology studies suggest that several of the metamorphic belts hosting these goldfields have a complex tectono-thermal history spanning multiple orogenic cycles (e.g., Boniface et al., 2012, Boniface and Schenk, 2012). As a result, linking deformation, magmatism, and mineralization to a particular orogenic cycle is equivocal in the absence of precise geochronologic constraints. In this contribution, we report new U-Pb titanite age constraints on the earliest deformation fabrics ("D1" – see below)

recognized within the western Lupa Goldfield, SW Tanzania. Together the available data suggest that Proterozoic-Palaeozoic metamorphic belts surrounding the Archaean Tanzanian Craton represent highly prospective regions and possess hitherto unrecognized gold potential.

*1.2 Chronology of gold deposits hosted by metamorphic belts*

Determining the absolute ages of magmatism, metamorphism and mineralization at gold deposits hosted by metamorphic belts is the subject of concentrated study and continuing controversy (e.g., Groves et al., 2003). Establishing the timing of mineralization is particularly challenging due to the dearth of suitable minerals for traditional geochronologic methods. Nevertheless, recent advances in unconventional sulphide (Stein et al., 2000; Morelli et al., 2007), hydrothermal phosphate (Şener et al., 2005; Vielreicher et al., 2010) and titanite (Lin and Corfu, 2002) geochronometers has dramatically improved our understanding of metallogenic time scales and processes at paleo-convergent margins. Re-Os geochronology studies (i.e., Re-Os dating of sulphide minerals presumed to be co-genetic with gold) have proven to be a particularly effective approach and have provided unequivocal examples of gold mineralization concomitant with magmatic intrusions at the million-year time scale (Morelli et al., 2007; Ootes et al., 2007; 2011; Lawley et al., in press-a). These studies add to a rapidly expanding global database of geochronologic ages that demonstrate broad contemporaneity between the absolute timing of gold and magmatism at most world-class goldfields (e.g., Witt and Vanderhor, 1998; Kerrich and Wyman, 1990; Kerrich and Cassidy, 1994; Kerrich and Kyser, 1994; Oberthur et al., 1998; Arne et al., 2001; Davis and Lin, 2003; Bucci et al., 2004; Bierlein et al., 2009; Dziggel et al., 2010; McFarlane et al., 2011).

The temporal relationship between magmatism and gold mineralization has led to the intrusion-related deposit model and is cited as evidence for the importance of locally derived magmatic hydrothermal fluids in the development of epigenetic gold deposits hosted by metamorphic belts at convergent margins (Sillitoe and Thompson, 1998; Lang and Baker, 2001). The inference of locally derived magmatic hydrothermal fluids is at odds with orogenic gold deposits, which are associated with a similar geodynamic setting (i.e., convergent margins), but are related to distal hydrothermal fluids of probable metamorphic origin (e.g., Groves et al., 1998; Groves et al., 2003; Phillips and Powell, 2010). Previous attempts at addressing this controversy have employed a variety of isotopic tracers, but have provided contrasting results due to, in part, the difficulty in discriminating isotopically distinct fluid sources after the fluid-rock interaction that characterizes most hydrothermal systems (e.g., Ridley and Diamond, 2000; Salier et al., 2005; Fu et al., 2012).

The recent emphasis placed on the role of metal-rich magmatic fluids emanating from mid- to lower-crustal magmatic systems also raises the possibility of distally (e.g., lower crustal) derived magmatic fluids contributing to hydrothermal systems operating at higher crustal levels (Botcharnikov et al., 2011; Hronsky et al., 2012). Whilst the genetic relationship between magmatic hydrothermal fluids and gold is satisfactorily demonstrated at several deposits (e.g., Hemlo; Davis and Lin, 2003), the exact role of magmatism and magmatically derived hydrothermal fluids in the development of epigenetic gold mineralization remains uncertain at most metamorphic belts (e.g., Charter Towers; Kreuzer, 2005). However, precise geochronologic constraints on magmatism and mineralization in conjunction with isotopic and fluid inclusions studies remain important tools in further constraining ore deposit models (Rasmussen et al., 2006).

Gold deposits and prospects in the Lupa Goldfield occur within a Palaeoproterozoic magmatic arc at the Tanzanian cratonic margin and thus share a close spatial and temporal relationship with granitic-gabbroic intrusions (Manya, 2011; Lawley et al., 2013). This spatial and temporal association between magmatism and mineralization has led to the suggestion that the gold prospects of the Lupa Goldfield are typical of the intrusion-related deposit type (Manya, 2012). In contrast, the protracted hydrothermal history (Lawley et al., in press-a) coupled with the structural setting of the deposits (Lawley et al., in press-b) suggests that these deposits share more similarities with orogenic style gold mineralization. In this contribution we report new U-Pb titanite ages, which provide new constraints on the onset of deformation at the Lupa Goldfield. This, coupled with the available Re-Os and U-Pb ages allows a critical evaluation of ore deposit models for gold prospects within the Lupa Goldfield.

## 2.0 Regional Geology

### *2.1 Tanzanian Craton and contiguous metamorphic belts*

The Tanzanian Craton extends from central to northern Tanzania and into southwestern Kenya and southeastern Uganda (Fig. 1). Previous workers divided the Archaean Tanzanian craton into three ‘Systems’ (e.g., Cahen et al., 1984) or ‘Supergroups’ (e.g., Borg and Krogh, 1999): 1) the Dodoman of central Tanzania, which comprises high-grade gneiss, migmatitic rocks, and granitic-granodioritic intrusions; 2) the Nyanzian of northern Tanzania, which comprises greenschist-amphibolite facies meta-volcanic rocks, lesser meta-sedimentary successions and granitic intrusions; and 3) the Kavirondian, which unconformably overlies the Nyanzian and comprises greenschist-amphibolite facies meta-sedimentary successions (for additional details regarding the geology, age and nomenclature of the Tanzanian Craton readers

are referred to reviews by Clifford, 1970; Bell and Dodson, 1981; Cahen et al., 1984; Borg and Krogh, 1989; Borg and Shackleton, 1997). However, more recent geologic and geochronological data sets suggest that the Nyanzian System comprises multiple temporally and geochemically distinct volcano-stratigraphic sequences, which should not be regarded as a single stratigraphic package (Manya et al., 2006). Moreover, the Tanzanian Cratons's tectonic framework is likely more complex than previously suggested and can be further subdivided into thirteen broadly WNW-ESE trending superterranes [Fig. 1; East Lake Victoria Superterrane (ELVST); Mwanza-Lake Eyasi Superterrane (MLEST); Lake Nyanza Superterrane (LNST); Moyowosi-Manyoni Superterrane, (MMST); Dodoma Basement Superterrane (DBST); Dodoma Schist Superterrane (DSST); Eastern Ubendian-Mtera Superterrane (EUMST); Kalenge-Burigi (KBST; not shown); Tectonic Front (TF; not shown); Mbulu-Masai Superterrane (MAST); Kilindi-Handeni Superterrane (KHST); Usagara-Ukaguru Superterrane (UKST); Uluguru-Pare Superterrane (UPST); Kabete et al., 2012a, b]. Although portions of this proposed tectonic framework require validation, the proposed model provides a potential explanation for the heterogeneous gold endowment within the Tanzanian Craton (for more details see Kabete et al., 2012a, b).

The newly defined tectonic subdivisions also provide a paradigm with which to explain the extension of gold-enriched superterranes into the metamorphic belts surrounding the Tanzanian Craton (Kabete et al., 2012a). To the east, the Tanzanian Craton is mantled by the Neoproterozoic-Palaeozoic East African Orogen (850–550 Ma, including the 650–620 Ma and ca. 550 Ma Mozambique Belt; e.g., Sommer et al., 2005a; Fritz et al., 2005; Thomas et al., 2013). The southern and western Tanzanian cratonic margins are bordered by the Palaeoproterozoic Usagaran and Ubendian Belts, respectively (2.1–1.8 Ga; e.g., Lenoir et al., 1994; Möller et al., 1998; Reddy et al., 2003; Boniface et al., 2012; Boniface and Schenk 2012). Finally, the northwestern margin of the Tanzanian Craton is bordered by the Mesoproterozoic Karagwe-Ankole Belt (ca. 1375 Ma; formally known as the Kibaran Belt; see De Waele et al., 2003, 2006, 2009; Tack et al., 2010 and Fernandez-Alonso et al., 2012 for recent discussions). In reality, each metamorphic belt is likely poly-orogenic and comprises, in part, reworked Archaean-Proterozoic crust. The details of this complex tectonic evolution is only beginning to emerge and only the Ubendian Belt, which hosts the Lupa Goldfield, is discussed in detail below.

*2.2 Ubendian Belt*

The Palaeoproterozoic Ubendian Belt is over 600 km long and ca. 150 km wide and comprises granulite-greenschist facies igneous and sedimentary rocks enveloping the western margin of the Tanzanian Craton. The NW-SE trending Ubendian Belt extends into northern

Malawi and Zambia and separates the Tanzanian and Congo Cratons. The belt is divided into eight litho-tectonic terranes (Katuma, Ikulu, Ubende, Wakole, Ufipa, Nyika, Upangwa, and Lupa; Daly, 1988) that are each separated by prominent NW-SE trending and steeply dipping shear zones (Fig. 2). The Palaeoproterozoic tectonic evolution of the belt is divided into two temporally distinct tectonic phases (Lenoir et al., 1994). The earliest of these tectonic phases, the 2.1–2.0 Ga Palaeoproterozoic Ubendian tectonic phase, is characterized by rare granulite facies tectonites and is considered to record the initial collision between the Tanzanian and Congo Cratons (Lenoir et al., 1994). This early Ubendian tectonic phase is overprinted by the second and younger 1.9–1.8 Ga Ubendian tectonic phase that resulted in the characteristic amphibolite-greenschist facies metamorphism and the NW-SE trending terrane-bounding shear zones (Lenoir et al., 1994). However, more recent work has identified disparately younger Mesoproterozic (ca. 1.09 Ga; Boniface et al., 2012) and Neoproterozoic-Palaeozoic (593–524 Ma; Boniface and Schenk, 2012) metamorphic events potentially related to the Irumide (1.05–1.00 Ga; De Waele et al., 2009) and Pan-African Orogens (950–450 Ma; Kröner, 1984; Stern, 1994). Neoproterozoic-Palaeozoic eclogite facies rocks dated at ca. 593, 548, 523 Ma provide particularly compelling evidence for disparately younger and previously unrecognized paleo-sutures within the Palaeoproterozoic Ubendian Belt (Boniface and Schenk, 2012). Together the available ages suggest that the Ubendian Belt is the product of at least three temporally discrete orogenic episodes. Moreover, later rifting associated with the western branch of the East African Rift, also likely contributed to the current geometry of the Ubendian Belt (Theunissen et al., 1996). The metallogenic implications of these overprinting metamorphic events are discussed further below.

## 2.0 Local Geology

### *2.1 Geology of Lupa Goldfield*

The field area for the current study is located in the western portion of the Lupa Goldfield, SW Tanzania (Figs. 1−3). Previously reported U-Pb and Re-Os ages are summarized in Fig. 4 and Table 1. Foliated Archaean granites (2.76–2.72 Ga) are cut by non-foliated Palaeoproterozoic granites and dioritic-gabbroic intrusions (1.96–1.88 Ga; Lawley et al., 2013). Archaean granites are generally coarse grained, equigranular to porphyritic (K feldspar phenocrysts) and represent a range of modal mineralogy (syeno- to monzogranite) and compositions (Lawley et al., 2013). Primary Fe-Mg minerals have been variably replaced to a chlorite ± epidote ± muscovite ± calcite ± titanite ± magnetite mineral assemblage.

The oldest tectonic fabric (D1), which is the focus of this study, is largely restricted to these Archaean granites and is characterized by alternating quartzofeldspathic and chloritic folia

that locally gives the granites a "gneiss-like" appearance (see legend of Fig. 3; Kimambo, 1984). The compositional banding is generally steeply dipping and varies in strike from E-W to NW-SE, but the fabric orientation and intensity can vary remarkably at the scale of individual outcrops. Cross cutting and overprinting relationships observed in drill core and outcrops imply that the D1 fabric, at least locally, preceded the emplacement of Palaeoproterozoic and non-foliated intrusions (i.e., D1 is locally ≥1.96 Ga). However, exposures of the Ilunga Syenogranite (ca. 1.96 Ga) at the Dubwana exploration target (Fig. 4) locally exhibit compositional banding (i.e., alternating quartzofeldspathic and chloritic folia) akin to the D1 fabric observed in Archaean granites and may suggest that D1 occurred diachronously during Palaeoproterozoic magmatism (discussed further below).

We expect that the D1 foliation developed at greenschist facies metamorphic conditions based on the chlorite ± muscovite ± epidote ± calcite metamorphic mineral assemblage and the dominant deformation microstructures (e.g., undulose extinction of quartz; crystal plastic deformation of quartz; Lawley et al., in press-b), which are typical of mid-crustal levels (300–450ºC; 1–3 kbar; Scholz, 1988). However, these inferred P-T conditions are notably lower than the amphibolite facies metamorphism that characterizes the other Ubendian Terranes and contrast with the "Acid Gneiss and Schist" lithologies that are reported to constitute large swaths of the Lupa Goldfield (Fig. 3; Kimambo, 1984). The field area for the current study (Fig. 4) is also devoid of 'acid volcanic rocks' and we suggest that the Lupa Goldfield geology map should be treated with caution (Fig. 3).

Palaeoproterozoic granitic-gabbroic intrusions in the Lupa Goldfield represent part of a voluminous magmatic arc at the Tanzanian cratonic margin (Figs. 2−4; see Manya, 2011 for further details). Two of these granites, the Saza Granodiorite and the Ilunga Syenogranite, are regionally extensive and are exposed across large tracts of the Lupa Goldfield and the field area for the current study (Figs. 3, 4). The Ilunga syenogranite (1960 ± 1 Ma; Lawley et al., 2013) is exposed in the northern portion of the field area and consists of a coarse grained and equigranular mineral assemblage of K feldspar ± quartz ± plagioclase with lesser amount of chloritized biotite. In contrast, the Saza Granodiorite (1935 ± 1 Ma; Lawley et al., 2013) is exposed in the southern portion of the field area and is characterized by a coarse grained and equigranular mineral assemblage of plagioclase ± quartz ± K feldspar with lesser amounts of chloritized hornblende ± biotite. Both granitoids possess dioritic-gabbroic enclaves and are also cut by dioritic-gabbroic dikes, which together suggest that intermediate-mafic magmatism pre- and post-dated the granitic intrusions. All magmatic phases in the field area have experienced greenschist facies metamorphism and are cut by D2 brittle-ductile and mylonitic shear zones (discussed further

below). Later brittle faults cutting mineralized structures (D3) and faults filled with unconsolidated gouge likely record younger, but undated deformation event(s) that may be related to periodic reactivation of Palaeoproterozoic structures to the present day (Theunissen et al., 1996).

*2.2 Gold Deposit Geology*

Most of the exposed gold deposits and prospects are hosted by steeply south-dipping D2 quartz veins and greenschist facies mylonitic shear zones (Figs. 4, 6a–c). The majority of these are associated with the ENE-WSW trending Saza shear zone and two other dominant structural trends (NW-SE and E-W; Fig. 4). The Kenge and Mbenge deposits, which are broadly representative of the majority of prospects studied, contain a measured and indicated resource of 8.7 Mt at 1.33 g/t gold with a 0.5 g/t cut-off resulting in an estimated 0.37 Moz of contained gold (Simpson, 2012). The deposits are hosted, in part, by mylonitic shear zones cutting foliated Archaean granite (e.g., Fig. 6a). Hydrothermal alteration, strain and mineralization at these deposits are largely restricted to the host shear zone and associated laminated-quartz (± carbonate) veins (Fig. 6c), whereas quartz veins outside of the main shear zone represent a relatively minor contribution to the overall mineral resource.

Recent drilling by Helio Resource Corp. has identified a second, geologically distinct, style of mineralization (e.g., Porcupine) that comprises a moderately to steeply dipping panel of narrow and discontinuous mylonitic shear zones separated by non-foliated, but hydrothermally altered (sericitized and silicified) and veined granite (Fig. 6d, e). The Porcupine deposit contains a measured and indicated resource of 15.4 Mt at 1.31 g/t gold with a 0.5 g/t cut-off for an estimated 0.65 Moz of contained gold (Simpson, 2012). The highest gold grades (e.g., up to 40 g/t Au) at Porcupine are associated with shallow dipping quartz veins and intervals of sericitized, silicified and non-foliated Ilunga syenogranite (Fig. 6d, e). These auriferous and shallow dipping quartz veins primarily occur within the moderately to steeply dipping panel of hydrothermally altered granite and significantly widen the mineralized zone at Porcupine, but are notably absent at Kenge and Mbenge. Regardless of the deposit style, gold is associated with a relatively simple sulphide mineral assemblage of pyrite ± chalcopyrite ± molybdenite ± galena ± sphalerite.

*2.3 Timing of Gold Mineralization*

Five gold deposits and prospects were sampled for Re-Os geochronology (Fig. 4; Lawley et al., in press-a). Individual Re-Os molybdenite, pyrite and chalcopyrite model ages range from 1.95–1.88 Ga and are thus broadly contemporaneous with the entire 1.96–1.88 Ga magmatic

history and the 1.9–1.8 Ga Ubendian tectonic phase (Fig. 5; Table 1). The absolute timing of gold within this temporal framework remains equivocal since gold is preferentially concentrated along pyrite crystal boundaries and locally occurs as pyrite fracture fills. These paragenetic relationships may provide evidence for a relatively late, and undated, gold event (Lawley et al., in press-a). Nevertheless, gold is observed as inclusions within ca. 1.88 Ga pyrite hosted by the main greenschist facies mylonitic shear zone at Kenge. This proposed ca. 1.88 Ga event is also recorded at all four of the other dated prospects (Mbenge, Porcupine, Konokono, and Dubwana). The paragenetic relationship between gold and these ca. 1.88 Ga pyrite and/or chalcopyrite samples at the other dated prospects is less clear, but the majority of samples were chosen from mineralized intervals and we suggest that the broad overlap of Re-Os sulphide ages between deposits and across the study area argues for a regional metallogenic event at ca. 1.88 Ga.

Disparately older ca. 1.95 and 1.94 Ga Re-Os molybdenite and pyrite model ages at Kenge were sampled from laminated and auriferous quartz veins hosted within the main mylonitic shear zone. The paragenetic relationship between gold and these sulphide samples is unclear and it remains equivocal whether: 1) the ca. 1.88 Ga gold event merely represents the youngest metallogenic event within a protracted (1.95–1.88 Ga) hydrothermal and progressive deformation history; or 2) the anomalously older Re-Os ages provide evidence for a telescoped deposit whereby the gold event at ca. 1.88 Ga merely overprints earlier, but unrelated style(s) of mineralization. Unfortunately the available ages and the ambiguous gold paragenesis do not allow us to rule out either of these possibilities. Nonetheless, the range of Re-Os ages suggest that laminated quartz veins possess protracted hydrothermal histories characterized by overprinting sulphidation events and that hydrothermal activity, at least locally, preceded the development of D2 mylonitic shear zones (Lawley et al., in press-a).

## 3.0 U-Pb titanite ID-TIMS Geochronology

### *3.1 Sample selection*

Foliated Archaean granites, such as the one selected for this study (sample CL109; U-Pb zircon La-ICP-MS weighted average $^{207}Pb/^{206}Pb$ age 2757 ± 10 Ma; Table 1; Lawley et al., 2013), are characterized by alternating quartzofeldspathic and chlorite-rich folia that developed during D1. Titanite crystals are concentrated within the D1 chlorite-rich folia and the greenschist facies metamorphic assemblage of chlorite ± epidote ± calcite ± titanite overprinting the protolith's Fe-Mg minerals (Figs. 7a, c). The petrographic association of titanite with the tectonic fabric and metamorphic mineral assemblage is consistent with titanite neo-crystallization during greenschist

306 facies metamorphism (Essex and Gromet, 2000; Frost et al., 2001; Parrish, 2001). This mineral
307 association is particularly apparent for the least-deformed examples of Archaean granites where
308 mineral dissolution and volume loss is unlikely to explain the apparent concentration of
309 metamorphic minerals. Moreover, euhedral titanite crystals isolated from the metamorphic
310 mineral assemblage were not observed and suggests that any igneous titanite, which would be
311 expected given the granitic composition, may have been recrystallized during subsequent
312 metamorphism. The nature of the metamorphic phase transition is unclear, but could be related to
313 the breakdown of primary clinopyroxene and/or amphibole by the hydration reaction
314 clinopyroxene + ilmenite + quartz + $H_2O$ = amphibole + titanite and/or the oxidation reaction
315 amphibole + ilmenite + $O_2$ = titanite + magnetite + quartz + $H_2O$ (Harlov et al., 2006).
316 Metamorphic reactions such as these are postulated to play an important role during metamorphic
317 titanite crystallization at greenschist facies P-T conditions (Frost et al., 2001).
318 Primary Fe-Mg minerals of the non-foliated Palaeoproterozoic Saza Granodiorite (sample
319 CL1035; U-Pb zircon ID-TIMS weighted average $^{207}Pb/^{206}Pb$ age at 1935 ± 1 Ma; Lawley et al.,
320 2013) are also replaced to a greenschist facies metamorphic mineral assemblage of chlorite ±
321 epidote ± calcite ± titanite. The association of titanite with this metamorphic mineral assemblage
322 is also consistent with titanite neo-crystallization during greenschist facies metamorphism,
323 however euhedral titanite crystals isolated from the metamorphic mineral assemblage may
324 represent relict magmatic titanite (Fig. 7d). Multiple titanite populations are characteristic of
325 metamorphosed lithologies and are typically distinguished through a combination of
326 optical/chemical characteristics and/or comparison of titanite ages with independent estimates for
327 the crystallization age of the sample (Jung and Hellebrand, 2007). In this contribution, we follow
328 a similar approach and compare new U-Pb titanite ages with previously reported U-Pb zircon
329 ages for the same samples.
330 The titanite crystals present within the bulk mineral separate from sample CL109 and
331 CL1035 are translucent, range in colour from brown to clear, and are present as broken fragments
332 and fine-grained wedge-shaped crystals. For sample CL109, clear and relatively fine grained
333 titanite crystals devoid of inclusions were chosen (Fig. 7e); whereas relatively much larger clear-
334 brown titanite crystals devoid of inclusions from sample CL1035 were selected for U-Pb ID-
335 TIMS analysis (Figs. 7f). The significance of these visually distinct titanite fractions is discussed
336 further below.
337

338 *3.2 Sample Preparation and ID-TIMS Methodology*

All of the analysed titanite crystals were ultrasonically cleaned for an hour before being placed on a hotplate for 30 minutes, photographed in transmitted light and rinsed in ultrapure acetone. After rinsing, titanite fractions were transferred to 300 µl Teflon FEP microcapsules and spiked with a mixed $^{233}U$–$^{235}U$–$^{205}Pb$ tracer. Titanite crystals were then dissolved in ~120 µl of 29 M HF with a trace amount of 30% $HNO_3$ within microcapsules, placed in Parr vessels at ~220°C for 48 hours, dried to fluorides and then converted to chlorides at ~180°C overnight. U and Pb for all titanite fractions were separated using standard HBr and $HNO_3$-based anion-exchange chromatographic procedures. Isotope ratios were measured at the NERC Isotope Geosciences Laboratory (NIGL), UK, using a Thermo-Electron Triton Thermal Ionisation Mass-Spectrometer (TIMS). Pb and U were loaded separately on a single Re filaments in a silica-gel/phosphoric acid mixture. Pb was measured by peak hopping on a single SEM detector. U isotopic measurements were made in static Faraday mode. Age calculations and uncertainty estimation (including U/Th disequilibrium) was based upon the algorithms of Schmitz and Schoene (2007) and Crowley et al. (2007), using the updated consensus value of $^{238}U/^{235}U = 137.818 \pm 0.045$ (Hiess et al., 2012) and the decay constant and its uncertainty of Jaffey et al. (1971).

## 4.0 U-Pb titanite ID-TIMS results and interpretation

### *4.1 Common lead correction*

Titanite crystals can incorporate significant concentrations of common lead during crystallization, which must be corrected for in order to determine accurate U-Pb ages (e.g., Frost et al., 2001). In general, the available approaches to common lead correction can be divided into three broad categories: 1) measure the lead isotopic composition of co-genetic and low-U phases, such as feldspar, and assume this isotopic composition is equivalent to common Pb at the time of titanite crystallization; 2) apply lead isotopic evolution models, such as the two-stage lead evolution model of Stacey and Kramers (1975; S-K model), and assume that this composition is equivalent to the isotopic composition of common Pb at the time of titanite crystallization; and 3) utilize regression techniques, such as the 'Total Pb/U isochron', which requires no *a priori* assumption of the common lead's isotopic composition (Ludwig, 2008).

The analysis of low-U mineral phases (e.g., feldspar) was deemed inappropriate for our data set since titanite crystals occurs with the metamorphic mineral assemblage and is therefore unlikely to be in isotopic equilibrium with igneous feldspar. Furthermore, previous Pb isotopic studies have demonstrated complex Pb isotopic systematics of feldspar (and galena) for samples

taken from the Ubendian and Usagaran Belts, which likely reflects metamorphic overprinting and open system behavior during multiple orogenic cycles at the Tanzanian cratonic margin (e.g., Möller et al., 1998). The 'Total Pb/U Isochron' (Ludwig, 1998; Ludwig, 2008) makes no *a priori* assumption as to the isotopic composition of common Pb and, providing the data set represents a suite of co-genetic and undisturbed titanite fractions that share a common Pb isotopic composition, represents a robust approach to common lead correction (e.g., Corfu and Stone, 1998; Storey et al., 2006). Unfortunately, titanite fractions from CL109 and CL0975 show evidence of disturbance to the U-Pb systematics (discussed further below) and so for the remaining discussion common lead for both samples was corrected by employing the S-K model approach. The sensitivity of the analyzed titanite fractions to the S-K model common lead correction is discussed further below.

### *4.2 U-Pb titanite ID-TIMS results and interpretation*

#### *4.2.1 Archaean Granite (CL109)*

U-Pb titanite data are reported in Table 2 and Fig. 8. For the foliated Archaean granite (sample CL109), nine titanite fractions yield $^{238}U/^{204}Pb$ and $^{206}Pb/^{204}Pb$ ratios ranging from 110–545 and 40–190, respectively. Common lead is significant for this dataset as suggested by the low $Pb^*/Pb_c$ ratios (1–9; where Pb* and $Pb_c$ correspond to radiogenic and common lead, respectively). As a result, the choice of the isotopic composition of common lead can have a substantial impact on the calculated U-Pb ages. We tested the effect of the assumed common lead composition on titanite ages by varying the S-K model age composition from 2.5–1.5 Ga and found that some individual $^{207}Pb/^{206}Pb$ titanite ages varied considerably, whereas the weighted average $^{207}Pb/^{206}Pb$ titanite age of all the analyzed titanite fractions did not (weighted average $^{207}Pb/^{206}Pb$ ages range from 1943–1911 Ma; Fig. 8a inset). Titanite fractions S3 and S4 are considerably more sensitive to the assumed common lead composition and also possess anomalously younger $^{207}Pb/^{206}Pb$ ages for S-K model Pb compositions at 1.5 and 1.9 Ga, whereas the other seven titanite fractions were relatively insensitive to the S-K model lead isotopic composition and possess $^{207}Pb/^{206}Pb$ ages that overlap within analytical uncertainty at the 2σ level (Fig. 8a inset). As a result, the common lead isotopic composition was assumed by selecting the S-K model lead isotopic composition at 1.9 Ga, which we use as a reasonable first order approximation of its true value.

A conventional 2D Terra-Wasserburg regression of the seven common Pb corrected and insensitive titanite fractions yield a Model 1 York regression solution upper intercept age of 1921 ± 7 Ma (MSWD = 0.7; probability of fit = 0.6; n = 7; Fig. 8a). It is important to note, that these

403 Palaeoproterozoic ages for titanite are all considerably younger than the LA-ICP-MS weighted
404 average $^{207}Pb/^{206}Pb$ zircon age for the same sample (2757 ± 10 Ma; Fig. 8a; Lawley et al., 2013).
405 The geological significance of these Palaeoproterozoic titanite ages is discussed further below.
406
407 *4.2.2 Saza Granodiorite (CL0975)*
408 The five titanite fractions analyzed from the Saza Granodiorite (sample CL0975) possess
409 a range of $^{238}U/^{204}Pb$ and $^{206}Pb/^{204}Pb$ from 294–859 and 118–315, respectively. These ratios, and
410 in particular the relatively higher Pb*/Pbc ratios (5–13), suggest that titanite crystals from
411 CL0975 are more U rich and possess less common Pb than titanite analyses from CL109. We
412 tested the effect of the assumed common Pb composition on titanite ages, as above, by varying
413 the S-K model age composition from 2.5–1.5 Ga and found that individual $^{207}Pb/^{206}Pb$ titanite
414 ages and weighted average $^{207}Pb/^{206}Pb$ titanite ages were both relatively insensitive to the inferred
415 isotopic composition of common lead (weighted average $^{207}Pb/^{206}Pb$ ages range from 1942–1924
416 Ma; Fig. 8b inset). As above, the common lead isotopic composition was assumed by selecting
417 the S-K model lead isotopic composition at 1.9 Ga, which we expect is the best first order
418 approximation of its true value.
419 A conventional 2D Terra-Wasserburg regression of the five common Pb corrected titanite
420 fractions yield a Model 1 York regression solution upper intercept age of 1931 ± 3 Ma (MSWD =
421 1.1; probability of fit = 0.4; n = 5; Fig. 8b). This upper intercept regression age is comparable to
422 a weighted average $^{207}Pb/^{206}Pb$ age of the three concordant titanite fractions, which represent the
423 least disturbed titanite fractions, at 1930 ± 3 Ma (MSWD = 0.6; probability of fit = 0.5; n = 3).
424 Both the weighted average (based on the three concordant and thus least disturbed titanite
425 fractions) age and the 2D regression age (based on all of the analyzed titanite fractions) ages are
426 in excellent agreement with each other and are only slightly outside of analytical uncertainty at
427 the 2σ level with a high-precision ID-TIMS weighted average $^{207}Pb/^{206}Pb$ zircon age of 1935 ± 1
428 Ma (Lawley et al., 2013) for the same sample (Fig. 8b).
429
430 **5.0 Discussion**
431 *5.1 Geological significance of U-Pb titanite ages*
432 *5.1.1 Archaean Granite (CL109)*
433 Titanite crystals from the foliated Archaean granite sample (CL109) are spatially
434 associated with the metamorphic fabric/mineral assemblage and provide evidence for titanite neo-
435 crystallization related to the breakdown of primary Fe-Mg minerals during greenschist facies
436 metamorphism and the development of the D1 deformation fabric (Fig. 7). The generally low

437 $Pb^*/Pb_c$ ratios (1–9; Table 2) of the analyzed titanite fractions support this interpretation and are
438 consistent with the compositional characteristics (i.e., relatively high common lead and low U) of
439 metamorphic titanite reported in previous studies (e.g., Frost et al., 2001; Jung and Hellebrand,
440 2007). Whilst the precise age of titanite fractions from CL109 remains open to interpretation due
441 to, in part, the sensitivity of U-Pb ages to the assumed isotopic composition of common lead,
442 these new U-Pb data clearly show that titanite crystals are in fact Palaeoproterozoic and therefore
443 considerably younger than Archaean U-Pb zircon ages for the same sample (Fig. 8a; Table 1).
444 Sample CL109 is cut by a non-foliated gabbroic dyke that is dated by LA-ICP-MS U-Pb
445 zircon geochronology at ca. 1.88 Ga (Lawley et al.,2013), which is consistent with the ca 1.92 Ga
446 U-Pb titanite age interpreted to date the timing of D1. However, elsewhere foliated Archaean
447 granites are cut by ca. 1.96 Ga granodioritic-granitic dykes and intrusions (most notably the 1960
448 ± 1 Ma Ilunga Syenogranite; Lawley et al., 2013), which is significantly older (ca. 40 Myr older
449 than the upper Concordia intercept age at 1921 ± 7 Ma ; Fig. 8a) than the inferred D1 timing
450 reported here. This suggests either: 1) D1 is more complex than previously thought and
451 developed diachronously during Palaeoproterozoic magmatism (Fig. 9); and/or 2) that U-Pb
452 titanite dates from sample CL109 are younger than their true age as a result of Pb-loss and/or
453 inappropriate common Pb correction (Fig. 8b). The latter is supported by the absence of a ductile
454 deformation fabric within the Saza Granodiorite (ca. 1.93 Ga), which would be expected if D1
455 had occurred at ca. 1.92 Ga (Fig. 9e). Alternatively, the D1 fabric may have developed
456 episodically during the emplacement of Palaeoproterozoic granites, which is consistent with
457 compositional banding akin to the D1 fabric observed in Archaean granites, but locally observed
458 in the Ilunga Syenogranite at Dubwana.
459 The current data set does not allow us to rule out either of these possibilities and thus the
460 precise timing of D1 deformation remains unclear. Nevertheless, these new U-Pb titanite ages
461 provide new evidence to suggest that the earliest identifiable deformation event in the Lupa
462 Goldfield occurred during the Palaeoproterozoic and some 40 Myr prior to D2 mylonitic shear
463 zones and gold at ca. 1.88 Ga. This extended Palaeoproterozoic structural history places
464 important new constraints on the onset of deformation related to Ubendian orogenesis and raises
465 the possibility that fabric development during D1 may have played an important role in localizing
466 strain during later deformation (see below for further discussion).
467
468 *5.1.2 Saza Granodiorite (CL0975)*
469 Titanite crystals from the non-foliated Saza granodiorite (sample CL0975) are locally
470 associated with the greenschist facies mineral assemblage overprinting the Saza Granodiorite and

thus exhibit textural similarities in thin section to titanite crystals extracted from the foliated Archaean granite (sample CL109). However, titanite crystals isolated from the Saza Granodiorite are visually distinct (i.e., larger and are brown-translucent), which suggests that these titanite crystals may represent a titanite population dissimilar to metamorphic titanite observed in sample CL109 (Figs. 7e, f). The higher $^{206}Pb/^{238}U$ ratios and generally higher $Pb^*/Pb_c$ ratios (5–13; Table 2) within the analyzed titanite fractions from the Saza Granodiorite are also unlike titanite fractions from the foliated Archaean granite and are more consistent with the more radiogenic composition of magmatic titanite (e.g., Jung and Hellebrand, 2007).

The weighted average $^{207}Pb/^{206}Pb$ titanite age of the three concordant titanite analyses (1930 ± 3 Ma) are slightly outside of analytical uncertainty of the weighted average $^{207}Pb/^{206}Pb$ zircon age (1935 ± 1 Ma) of concordant zircons for the same sample and support a magmatic origin for the analyzed titanite fractions. The broad agreement between both geochronometers suggests that the Stacey and Kramers (1975) common lead correction approach is broadly appropriate despite two of the common lead corrected titanite fractions exhibiting severe reverse discordance (Fig. 8b). The cause of reverse discordance is unclear and could be related to U loss and/or represent an analytical effect. The slight discrepancy between the interpreted crystallization age and U-Pb titanite ages could be related to minor Pb-loss in the analyzed titanite fractions, later closure during cooling, sub-solidus recrystallization, and/or inadequate accounting for the common lead correction (Frost et al., 2001). If the nominally younger U-Pb titanite ages represent cooling ages, our results would suggest that the Saza Granodiorite cooled relatively quickly since U-Pb titanite and zircon ages are only <1 Myr outside of analytical uncertainty at the 2σ level.

*5.2 Implications for ore deposit models*

Here we integrate new U-Pb titanite ages with previously reported U-Pb and Re-Os ages to address some of the outstanding uncertainties (e.g., the temporal relationship between D1 and D2) at gold prospects within the Lupa Goldfield. At least three temporally distinct hydrothermal events have been identified in the Lupa Goldfield (1.95, 1.94 and 1.88 Ga; Lawley et al., in press-a; Fig. 5). Gold is expected to have been introduced at ca. 1.88 Ga, whereas the relationship between gold and disparately older Re-Os model ages at ca. 1.95 Ga and 1.94 Ga is less clear. Each of these broadly defined hydrothermal events are represented in detail by complex vein histories that suggest each event occurred at a time scale that is less than the resolution of the Re-Os method. This episodic, but protracted hydrothermal history (1.95–1.88 Ga) overlaps with the Palaeoproterozoic magmatic history of the Goldfield as determined by U-Pb zircon dating of

505 felsic-mafic intrusions/dykes (1.96–1.88 Ga; Fig. 5). Furthermore, high-precision U-Pb zircon
506 ID-TIMS ages for the Saza Granodiorite (1935 ± 1 Ma) overlap with Re-Os molybdenite ages
507 (ca. 1.94 Ga) and provide unequivocal evidence for sulphidation that is concomitant with
508 magmatism at the million-year time scale.
509 This close temporal relation has led to the suggestion that gold deposits within the Lupa
510 Goldfield belong to the intrusion-related ore deposit type (Manya, 2012). However, Re-Os model
511 ages pre- and post-date individual magmatic phases and hydrothermal activity appears to have
512 occurred at a time scale that is far greater than the expected duration of a single magmatically
513 derived hydrothermal fluid circulation system (e.g., <1 Myr; von Quadt et al., 2011). Moreover,
514 the proposed gold event at ca. 1.88 Ga is disparately younger than any of the dated granites and
515 we suggest that a simple intrusion-related deposit model (e.g., Manya, 2012) whereby
516 metalliferous and hydrothermal fluids exsolving from the Saza Granodiorite are solely
517 responsible for gold is unsupported.
518 New U-Pb titanite ages reported here further constrain ore deposit models by
519 demonstrating that the onset of deformation occurred during the Palaeoproterozoic. It further
520 suggests that deformation was progressive and broadly overlaps with Palaeoproterozoic
521 magmatism (Figs. 5, 9). The broad temporal overlap between hydrothermal (1.95–1.88 Ga),
522 magmatic (1.96–1.88 Ga) and deformation (≥1.92–1.88 Ga) events in the Lupa Goldfield are also
523 well correlated to the tectono-thermal history recorded by the other Ubendian Terranes (i.e., the
524 2.1–1.8 Ga Ubendian Orogeny and specifically the 1.9–1.8 Ga Ubendian tectonic phase; Lenoir et
525 al., 1994). In particular, the Palaeoproterozoic MORB-like chemistry eclogites (ca. 1.89 and 1.86
526 Ga; Boniface et al., 2012) sampled from the Ubende Terrane demonstrates that high-grade
527 metamorphism related to subduction of oceanic crust broadly overlaps with the proposed gold
528 event at ca. 1.88 Ga within the Lupa Goldfield. Palaeoproterozoic eclogitic rocks in the Ubende
529 Terrane are amongst the oldest eclogites on Earth (Boniface et al., 2012) and therefore represent a
530 key link between metallogenesis related to modern and ancient subduction zone processes. A
531 holistic understanding of Ubendian tectonics requires additional constraints on the significance
532 and distribution of Meso- and Neoproterozoic metamorphic overprints. Nevertheless, the link
533 between Palaeoproterozoic convergent tectonics, subduction zone processes and gold
534 mineralization in the Lupa Goldfield is implied.
535 The consistent sulphide mineralogy between gold prospects, in conjunction with a
536 comparable alteration mineral assemblage and overlapping sulphide ages, suggests that all of the
537 studied gold prospects are consanguineous and can be considered as part of the same broad
538 mineralization history related to an interconnected shear zone network that focused fluids at the

539 Tanzanian cratonic margin during Palaeoproterozoic Ubendian orogenesis. Together the timing,
540 structural setting and geological characteristics suggest that gold prospects exposed in artisanal
541 workings within the western Lupa Goldfield are typical of the orogenic gold deposit type [i.e.,
542 shear and quartz-carbonate vein hosted, sulphide poor and Au dominated deposits that result from
543 structural focusing of low salinity $H_2O$-$CO_2$ (± $CH_4$) fluids at convergent margins; *sensu* Groves
544 et al., 1998]. Our ages are also consistent with other palaeo-convergent margins where systematic
545 geochronology has demonstrated that orogenic style gold mineralization can occur throughout
546 orogenesis, but generally occurs relatively late during the orogen's tectono-thermal history (e.g.,
547 Sarma et al., 2011; Figs. 5, 9f).
548
549 *5.3 Archaean versus Proterozoic Tanzanian Gold Deposits*
550 In the preceding section we argue that gold deposits in the Lupa Goldfield share
551 similarities to the orogenic gold deposit type. In this section we compare and contrast the geology
552 of goldfields hosted within and at the margins of the Tanzanian Craton. The geologic
553 characteristics of deposits within each goldfield are taken from the available literature and are
554 summarized in Table 3. Overall, gold deposits within the Lake Victoria Goldfield share a number
555 of broad similarities with Palaeoproterozoic (e.g., ca. 1.88 Ga, Lupa), Mesoproterozoic (e.g., ca.
556 1.2 Ga, Mpanda; Kazimoto and Schenk, 2013), and Palaeozoic (e.g., ca. 483 Ma, Niassa;
557 Bjerkgard et al., 2009) goldfields situated within metamorphic belts marginal to the Tanzanian
558 Craton (Fig. 1). These gross geologic similarities include comparable hydrothermal alteration
559 mineral assemblages (sericite, chlorite, silica flooding, carbonate), sulphide mineral assemblages
560 (pyrite ± base-metal sulphides), metamorphic grade (amphibolite to greenschist) and similar
561 apparent controls on gold mineralization (predominately shear- and quartz vein-controlled and
562 lithologic contacts). However, in detail each deposit also possesses distinct geologic
563 characteristics that make direct comparisons between deposits — even within a single goldfield
564 — challenging. For example, the BIF-hosted Geita and intrusion-hosted Buzwagi deposits differ
565 from the other meta-sedimentary and –volcanic rocks hosted deposits in the Lake Victoria
566 Goldfield (Table 3).
567 Nevertheless goldfield comparisons such as those presented in Table 3 represent an
568 important exercise since several of the metamorphic belts enveloping that Tanzanian Craton are
569 now recognized to comprise, in part, re-worked Archaean crust (Ubendian Belt, Kazimoto and
570 Schenk, 2013, Lawley et al., 2013; Usagaran, Sommer et al., 2005b; Mozambique Belt, Kröner et
571 al., 2003; Sommer et al., 2005a; Thomas et al., 2013). As a result, these metamorphic belts may
572 host Archaean gold deposits that have been subsequently re-worked during Palaeoproterozoic-

Palaeozoic orogenic episodes. Unequivocal examples of re-worked Archean deposits have not been documented in Tanzania, but represent hitherto unrecognized gold potential within Proterozoic-Palaeozoic metamorphic belts surrounding the Tanzanian Craton (Kabete et. al., 2012a). Moreover, orogenic gold deposits hosted by re-worked Archaean crust are scarce globally although the Mesozoic goldfields within the North China Craton may represent possible exceptions (Li et al., 2012).

Gold deposits within the Lupa goldfield provide other natural examples of this unusual deposit setting since the inferred ca. 1.88 Ga gold event is hosted, in part, by re-worked Archaean granitoids. Individual Mesoproterozoic Re-Os ages at ca. 1371 Ma and 1057−922 Ma (Lawley et al., in press-a) and inferred lead-loss events at 514−469 Ma (Lawley et al., 2013), although not directly related to gold in the Lupa goldfield, are potentially related to later overprinting during multiple and temporally-discrete orogenic cycles (ca. 1375 Ma, Karagwe-Ankole Belt; 1.05–1.00 Ga Irumide Orogeny; 950–450 Ma Pan African Orogeny). Preliminary U-Pb monazite ages at ca. 1.2 Ga provide evidence for a potential Mesoproterozoic gold event at the Mpanda goldfield, which is also hosted, in part, by Archaean rocks re-worked during Palaeo- and Mesoproterozoic tectono-thermal events (Kazimoto and Schenk, 2013). However, the precise age of the Mpanda goldfield remains unclear because previously reported Pb-Pb model ages provided evidence for a disparately younger gold event at ca. 720 Ma (Stendal et al., 2004). Neoarchean-Palaeozoic gold is also reported in the ca. 743 Ma Niassa Goldfield, which are interpreted to reflect Pan-African orogenic style gold mineralization in NW Mozambique (Bjerkgard et al., 2009). Similar Pan-African gold events are also reported in other countries bordering the Tanzanian Craton although the geologic setting of these deposits remains poorly understood (Burundi, Rwanada, Uganda; Brinckmann et al., 1994; Fernandez-Alonso et al., 2012).

The examples provided above suggest that the metamorphic belts bordering the Tanzanian Craton are prospective for orogenic style gold mineralization spanning at least three orogenic episodes. The available geochronologic database highlights the importance of robust geochronometers that remain closed during overprinting geologic events. It also stresses the need for robust geochronometers that record and, can be paragenetically linked to, different stages of the tectono-thermal history. The latter is particularly important in poly-orogenic settings where the enrichment or possible remobilization of gold through time is expected to be a key process for gold deposits hosted by metamorphic belts (Groves et al., 2003).

*5.4 Structural evolution of the Lupa Goldfield*

606 New U-Pb titanite ages from an Archaean granite sample (CL109) demonstrates the onset
607 of deformation in the Lupa Goldfield occurred during the Palaeoproterozoic and pre-dated D2
608 auriferous mylonites by ≥40 Myr. Here we suggest that foliated Archaean granites, developed
609 during D1, acted as zones of pre-existing structural weakness and/or heterogeneity and may have
610 played a key role in strain localization during later deformation. This is particularly apparent for
611 gold prospects hosted by D2 mylonitic shear zones developed within foliated Archaean granites
612 such as at Kenge and Mbenge (Fig. 6a). At these mineral systems, the orientation of mylonitic
613 shear zones closely follows the geometry of the D1 fabric (Lawley et al., in press-b). The sharp
614 contacts between the mylonitic shear zones and foliated wall rock suggests that the D1 fabric was
615 not passively re-oriented during subsequent deformation, and instead suggests D1 fabric acted as
616 a structural weakness and/or heterogeneity that localized strain during D2 (e.g., Fig. 6b).
617 However for several shear zones (e.g., Saza shear zone), and for those gold prospects hosted by
618 non-foliated Palaeoproterozoic intrusive phases, the importance of D1 deformation on the
619 development of auriferous shear zones is unclear.
620 Re-Os dating has also identified hydrothermal events (ca. 1.95 and 1.94 Ga; Lawley et
621 al., in press-a) that pre-date the timing of D1 reported as part of this study (ca. 1.92 Ga). These
622 anomalously older sulphides were sampled from laminated quartz veins filling and deformed by
623 D2 mylonitic shear zones at Kenge. The latter suggests that quartz veining may have in fact, at
624 least locally, pre-dated the D1 fabric (Fig. 9d). Unfortunately, the uncertainty in the common-lead
625 correction precludes a precise U-Pb titanite age for the onset of ductile deformation and does not
626 allow us to evaluate this possibility further. Nevertheless, structural preparation has been shown
627 to play an important role at goldfields where orogenic style gold mineralization is kinematically
628 late (Groves et al., 2000). Pre-existing structures, such as brittle faults and/or lithologic contacts,
629 are widely recognized as 'stress risers' that facilitate reactivation over the formation of new
630 structures at the deposit scale (e.g., Dubé et al., 1989; Lin and Corfu, 2002).
631 The importance of structural reactivation is also suggested by the link between orogenic
632 gold style mineralization, compressional to transpressional settings and "mis-oriented" high-angle
633 reverse shear zones (e.g., Sibson, 1988). In these geologic settings and in a compressional stress
634 regime, high-angle reverse faults are more likely to represent reactivation of pre-existing
635 structures due to high fluid pressure and/or low frictional fault strength rather than newly
636 developed structures (Lawley et al., in press-b). We suggest that D1 and, particularly the
637 development of planes comprising rheologically weak chloritic folia, created zones of structural
638 weakness that may have, at least locally, acted as pre-existing anisotropies that were potentially
639 reactivated during later D2 brittle-ductile deformation. The abundance of chlorite slickensides on

D1 chloritic folia, which are unlikely to have formed during the dominantly ductile D1 event(s), supports this interpretation and also suggests that early ductile deformation may have been reactivated during late brittle faulting (D3).

Together the available field relationships and absolute ages of deformation fabrics record a broad progression from dominantly D1 ductile (ca. 1.92), to D2 brittle-ductile auriferous mylonitic shear zones and quartz veins (ca. 1.88 Ga) and ultimately to D3 cataclasites and discrete faults during later, but undated, and dominantly brittle deformation. A similar progression in deformation characteristics, i.e. from dominantly ductile to brittle deformation, has also been reported in goldfields associated with more modern orogenic settings and has been attributed to changing P-T conditions during orogenic uplift, denudation and cooling (e.g., Alps; Pettke et al., 1999).

## 6.0 Conclusions

Titanite U-Pb geochronology for a foliated Archaean granite, which represents the earliest identifiable deformation event in the Lupa Goldfield, suggests that the onset of deformation occurred during the Palaeoproterozoic at ca. 1.92 Ga. This age raises new questions regarding the timing of the D1 fabric and suggests either: 1) titanite dates are slightly younger than their true age due to lead-loss or an inaccurate common lead correction; and/or 2) that D1 is more complex than previously recognized and occurred diachronously during the emplacement of Palaeoproterozoic intrusions. New U-Pb titanite ages for the non-foliated Saza Granodiorite at 1930 ± 3 Ma, are only nominally younger than the U-Pb zircon age (1935 ± 1 Ma) for the same sample.

These U-Pb titanite ages, combined with previously reported U-Pb zircon and Re-Os sulphide geochronology, constrain the Palaeoproterozoic timing of magmatism (1.96–1.88 Ga), hydrothermal activity (1.95–1.88 Ga) and deformation/metamorphism (≥1.92–1.88 Ga) in the Lupa Goldfield. Together the available geochronologic data demonstrate a progression from dominantly ductile (D1) to brittle-ductile deformation (D2) over ≥40 Myr, which occurred diachronously and intermittent with felsic-mafic plutonism during a Palaeoproterozoic orogenic cycle at the Tanzanian cratonic margin. However, the inferred ca. 1.88 Ga gold event in the Lupa Goldfield simply represents the earliest episode of orogenic gold deposit formation in western Tanzania and are superseded by younger orogenic gold style mineralization events related to temporally discrete orogenic episodes at cratonic margins bordering the Ubendian Belt. The Tanzanian cratonic margin is therefore highly prospective for orogenic style gold mineralization, which may have developed during multiple orogenic events.

**Acknowledgements**

CJML would like to thank funding provided by a Durham Doctoral Fellowship and a student research grant awarded by the Society of Economic Geologists. Helio Reosurce Corp. also provided funding, logistical support and access to the exploration licenses for sampling. The manuscript benefitted from critical reviews by Nicole Rayner, Richard Goldfarb and Joas Kabete. Emmanuel Kazimoto also improved the manuscript by providing additional details concerning the geology of the Mpanda and Lake Victoria Goldfields. Natural Resources Canada Earth Science Sector contribution No. 20130046.

**References**

AngloGold Ashanti Annual Report, 2012, www.anglogold.com, 125 p.

Arne, D.C., Bierlein, F.P., Morgan, W., Stein, H.J., 2001. Re-Os dating of sulfides associated with gold mineralization in central Victoria, Australia. Economic Geology, 96, 1455–1459.

Barrick Gold Corporation Annual Report 2012, www.africabarrickgold.com, 180 p.

Bell, K., Dodson, M.H., 1981. The geochronology of the Tanzanian Shield. The Journal of Geology, 89, 109−128.

Bierlein, F.P., Groves, D.I., Cawood, P.A., 2009. Metallogeny of accretionary orogens – the connection between lithospheric processes and metal endowment. Ore Geology Reviews, 36, 282–292.

Bjerkgard, R., Stein, H.J., Bingen, B., Henderson, I.H.C., Sandstad, J.C., Moniz, A., 2009. The Niassa Gold Belt, northern Mozambique – a segment of a continental-scale Pan-African gold-bearing structure? Journal of African Earth Sciences, 53, 45–58.

Boniface, N., Schenk, V., Appel, P., 2012. Paleoproterozoic eclogites of MORB-type chemistry and three Proterozoic orogenic cycles in the Ubendian Belt (Tanzania): Evidence from monazite and zircon geochronology, and geochemistry. Precambrian Research, 192–195, 16–33.

Boniface, N., Schenk, V., 2012. Neoproterozoic eclogites in the Paleoproterozoic Ubendian Belt of Tanzania: Evidence for a Pan-African suture between the Bangweulu Block and the Tanzania Craton. Precambrian Research, 208–211, 72–89.

Borg, G., Shackleton, R.M., 1997. The Tanzania and NE Zaire Cratons, In: Wit, M.J., Ashwal, L.D., (Eds.), Greenstone Belts. Clarendon Press, Oxford, p. 608–619.

Borg, G., Krogh, T., 1999. Isotopic age date of single zircons from the Archaean Sukumaland Greenstone Belt, Tanzania. Journal of African Earth Sciences, 29, 301–312.

Botcharnikov, R.E., Linnen, R.L., Wilke, M., Holtz, F., Jugo, P.J., Berndt, J., 2011. High gold concentrations in sulphide-bearing magma under oxidizing conditions. Nature Geoscience, 4, 112–115.

Brinckmann, J., Lehmann, B., Timm, F., 1994. Proterozoic gold mineralization in NW Burundi. Ore Geology Reviews, 9, 85−103.

Brown, T.J., Shaw, R.A., Bide, T., Petavratzi, E., Raycraft, E.R., Walters, A.S., 2013. World Mineral Production 2007−11, British Geological Survey, Keyworth, Nottingham, 85 p.

Bucci, L.A., McNaughton, N.J., Fletcher, I.R., Groves, D.I., Kositcin, N., Stein, H.J., Hagemann, S.G., 2004. Timing and duration of high-temperature gold mineralization and spatially associated granitoid magmatism at Chalice, Yilgarn Craton, Western Australia. Economic Geology, 99, 1123–1144.

Cahen, L., Snelling, N.J., Delhal, J., Vail, J., 1984. The Geochronology and Evolution of Africa, Clarendon Press, Oxford, 512 p.

Chamberlain, C.M., 2003. Geology and genesis of the Bulyanhulu gold deposit, Sukumaland greenstone belt. Unpublished PhD Thesis, Imperial College London, London.

Corfu, F., Stone, D., 1998. The significance of titanite and apatite U-Pb ages: Constraints for the post-magmatic thermal-hydrothermal evolution of a batholithic complex, Berens River

741 area, northwestern Superior Province, Canada. Geochimica et Cosmochimica Acta, 62,
742 2979–2995.
743
744 Crowley, J.L., Schoene, B., Bowring, S.A., 2007. U-Pb dating of zircon in the Bishop Tuff at the
745 millennial scale: Geology, 35, 1123–1126
746
747 Clifford, T.N., 1970. The structural framework of Africa, In: Clifford, T.N., and Gass, I., (Eds.),
748 African Magmatism and Tectonics. Oliver and Boyd, Edinburgh, 1–26.
749
750 Cloutier, J., Stevenson, R.K., Bardoux, M., 2005. Nd isotopic, petrological and geochemical
751 investigation of the Tulawaka East gold deposit, Tanzanian Craton. Precambrian Research,
752 139, 147−163.
753
754 Daly, M.C., 1988. Crustal shear zones in central Africa; a kinematic approach to Proterozoic
755 tectonics. Episodes, 11, 5–11.
756
757 Davis, D.W., Lin, S.F., 2003. Unraveling the geologic history of the Hemlo Archean gold deposit,
758 Superior province, Canada: a U-Pb geochronological study. Economic Geology, 98, p. 51–
759 67.
760
761 De Waele, Wingate, M.T.D., Fitzsimons, Mapani, B.S.WE., 2003. Untying the Kibaran knot: A
762 reassessment of Mesoproterozoic correlations in southern Africa based on SHRIMP U-Pb
763 data from the Irumide belt. Geology, 31, 509–512.
764
765 De Waele, B., Kampunzu, A.B., Mapani, B.S.E., Tembo, F., 2006. The Mesoproterozoic Irumide
766 belt of Zambia. Journal of African Earth Sciences, 46, 36–70.
767
768 De Waele, B., Fitzsimons, I.C.W., Wingate, M.T.D., Tembo, F., Mapani, B., 2009. The
769 geochronological framework of the Irumide Belt of Zambia: A prolonged crustal history
770 along the margin of the Bangweulu Craton. American Journal of Science, 309, 132–187.
771
772 Dubé, B., Poulsen, K.H., Guha, J., 1989. The effects of layer anisotropy on auriferous shear
773 zones: the Norbeau Mine, Quebec. Economic Geology, 84, 871–878.
774

775 Dziggel, A., Poujol, M., Otto, A., Kisters, A.F.M., Trieloff, M., Schwarz, W.H., Meyer, F.M.,
776 2010. New U-Pb and Ar-40/Ar-39 ages from the northern margin of the Barberton
777 greenstone belt, South Africa: Implication for the formation of Mesoarchaean gold
778 deposits. Precambrian Research, 179, 206–220.
779
780 Essex, R., Gromet, L.P., 2000. U-Pb dating of prograde and retrograde titanite growth during the
781 Scandian orogeny. Geology, 28, 419–422.
782
783 Fernandez-Alonso, M., Cutten, H., De Waele, B., Tack, L., Tahon, A., Baudet, D., Barritt, S.D.,
784 2012. The Mesoproterozoic Karagwe-Ankole Belt (formerly the NE Kibara Belt): The
785 result of prolonged extensional intracratonic basin development punctuated by two-short
786 lived far-field compressional events. Precambrian Research, 216–219, 63–86.
787
788 Fritz, H., Tenczer, V., Hauzenberger, C.A., Wallbrecher, E., Hoinkes, G., Muhongo, S.,
789 Mogessie, A., 2005. Central Tanzanian tectonic map: A step forward to decipher
790 Proterozoic structural events in the East African Orogen: Tectonics, 24, TC6013, 26 p.
791
792 Frost, B.R., Chamberlain, K.R., Schumacher, J.C., 2001. Sphene (titanite): phase relations and
793 role as a geochronometers. Chemical Geology, 172, 131−148.
794
795 Fu, B., Kendrick, M.A., Fairmaid, A.M., Phillips, D., Wilson, C.J.L., Mernagh, T.P., 2012. New
796 constraints on fluid sources in orogenic gold deposits, Victoria, Australia. Contributions to
797 Mineralogy and Petrology, 163, 427–447.
798
799 Goldfarb, R.J., Groves, D.I., Gardoll, S., 2001. Orogenic gold and geologic time: A global
800 synthesis. Ore Geology Reviews, 18, 1−75.
801
802 Groves, D.I., Goldfarb, R.J., Gebre-Mariam, M., Hagemann, S.G., Robert, F., 1998. Orogenic
803 gold deposits: A proposed classification in the context of their crustal distribution and
804 relationships to other gold deposit types. Ore Geology Reviews, 13, 7–27.
805
806 Groves, D.I., Goldfarb, R.J., Knox-Robinson, C.M., Ojala, J., Gardoll, S., Yun, G.Y., Holyland,
807 P., 2000. Late-kinematic timing of orogenic gold deposits and significance for computer-

based exploration techniques with emphasis on the Yilgarn Block, Western Australia. Ore Geology Reviews, 17, 1–38.

Groves, D.I., Goldfarb, R.J., Robert, F., Hart, C.J.R., 2003. Gold deposits in metamorphic belts: Overview of current understanding, outstanding problems, future research and exploration strategies. Economic Geology, 98, 1–29.

Harlov, D., Tropper, P., Seifert, W., Nijland, T., Forster, H.-J., 2006. Formation of Al-rich titanite ($CaTiSiO_4O$–$CaAlSiO_4OH$) reaction rims on ilmenite in metamorphic rocks as a function of $fH_2O$ and $fO_2$. Lithos, 88, 72–84.

Hiess, J., Condon, D. J., McLean, N., Noble, S. R., 2012. $^{238}U/^{235}U$ systematics in terrestrial uranium-bearing minerals. Science, 335, 1610-1614.

Hronsky, J.M.A., Groves, D.I., Loucks, R.R., Begg, G.C., 2012. A unified model for gold mineralization in accretionary orogens and implications for regional-scale exploration targeting methods. Mineralium Deposita, 47, 339–358.

Ikingura, J.R., Akagi, H., Mujumba, J., Messo, C., 2006. Environmental assessment of mercury dispersion, transformation and bioavailability in the Lake Victoria Goldfields, Tanzania. Journal of Environmental Management, 81, 167−173.

Ikingura, J.R., Mutakyahwa, M.K.D., Marobhe, I.M., Manya, S., Kazimoto, E.O., Mshiu, E.E., Charles, K., 2009. Atlas of gold deposits in Tanzania, 1st ed. University of Dar es Salaam, Dar es Salaam, Tanzania.

Jaffey, A.H., Flynn, K.F., Glendenin, L.E., Bentley, W.C., Essling, A.M., 1971. Precision measurement of half-lives and specific activities of $^{235}U$ and $^{238}U$. Physical Reviews C4, 4, 1889–1906.

Jung, S., Hellebrand, E., 2007. Textural, geochronological and chemical constraints from polygenetic titanite and monogenetic apatite from a mid-crustal shear zone: An integrated EPMA, SIMS, and TIMS study. Chemical Geology, 241, 88–107.

Kabete, J., 2008, A new terrane-based tectonic subdivision of the Archaean Craton and selected belts of Tanzania and its significance to gold metallogeny. PhD thesis, University of Dar es Salaam.

Kabete, J.M., Groves, D.I., McNaughton, N.J., Mruma, A.H., 2012a. A new tectonic and temporal framework for the Tanzanian Shield: Implications for gold metallogeny and undiscovered endowment. Ore Geology Reviews, 48, 88–124.

Kabete, J.M., McNaughton, N.J., Groves, D.I., Mruma, A.H., 2012b, Reconnaissance SHRIMP U-Pb zircon geochronology of the Tanzania Craton: Evidence for Neoarchean granitoid-greenstone belts in the Central Tanzania Region and the Southern East Africa Orogen. Precambrian Research, 216−219, 232−266.

Kazimoto, E., 2008. Study of integrated geochemical techniques in the exploration for gold in North Mara mines, Tanzania. Unpublished MSc. Thesis, University of Dar es Salaam, Dar es Salaam, 208 p.

Kazimoto, E., Schenk, V., 2013. Crustal evolution and hydrothermal gold mineralization in the Paleoproterozoic Katuma Block of the Ubendian Belt, Tanzania. The 24th Colloquium of African Geology, Conference Proceedings, January 8−14, Addis Ababa, Ethiopia.

Kerrich, R., Kyser, T.K., 1994. 100 Ma timing paradox of Archean gold, Abitibi greenstone-belt (Canada) – new evidence from U-Pb and Pb-Pb evaporation ages of hydrothermal zircons. Geology, 22, 1131–1134.

Kerrich, R., Cassidy, K.F., 1994. Temporal relationship of lode gold mineralization to accretion, magmatism, metamorphism and deformation – Archean to present: A review. Ore Geology Reviews, 9, 263–310.

Kerrich, R., Wyman, D., 1990. Geodynamic setting of mesothermal gold deposits: An association with accretionary tectonic regimes. Geology, 18, 882–885.

Kimambo, R.H.N., 1984, Mining and mineral prospects in Tanzania, Eastern Africa Publications Ltd., Arusha, 250 p.

Kreuzer, O.P., 2005, Intrusion-hosted mineralization in the charters towers Goldfield, North Queensland: New isotopic and fluid inclusion constraints on the timing and origin of the auriferous veins. Economic Geology, 100, 1583–1603.

Köner, A., 1984. Late Precambrian plate tectonics and orogeny: A need to redefine the term Pan-African, In: Klerkx, J., Michot, J., (Eds.), African Geology. Tervuren, Musée R. l'Afrique Centrale, 23–28.

Kröner, A., Muhongo, S., Hegner, E., Wingate, M.T.D., 2003. Single-zircon geochronology and Nd isotopic systematics of Proterozoic high-grade rocks from the Mozambique Belt of southern Tanzania (Masasi area): Implications for Gondwana assembly. Journal of the Geological Society, London, 160, 745−757.

Kuehn, S., Ogola, J., Sango, P., 1990. Regional setting and nature of gold mineralization in Tanzania and southwest Kenya. Precambrian Research, 46, 71−82.

Kwelwa, S., Manya, S., Vos, I.M.A., 2013, Geochemistry and petrogenesis of intrusions at the Golden Pride gold deposit in the Nzega greenstone belt, Tanzania. Journal of African Earth Sciences, 86, 53−64

Lang, J.R., Baker, T., 2001. Intrusion-related gold systems: The present level of understanding: Mineralium Deposita, 36, 477 – 489.

Lawley, C.J.M., Selby, D., Imber, J., in press-a, Re-Os molybdenite, pyrite and chalcopyrite geochronology, Lupa Goldfield, SW Tanzania: Tracing metallogenic time scale at mid-crustal shear zones hosting orogenic gold deposits. Economic Geology.

Lawley, C.J.M., Imber, J., Selby, D., in press-b, Structural controls on gold mineralization during transpression: Lupa Goldfield, SW Tanzania. Economic Geology.

Lawley, C.J.M., Selby, D., Condon, D., Morstwood, M., Millar, I., Crowley, Q., Imber, J., 2013, Lithogeochemistry, geochronology and geodynamic setting of the Lupa Terrane, Tanzania:

Implications for the extent of the Archean Tanzanian Craton. Precambrian Research, 231, 174−193.

Lenoir, J.L., Liégeois, J.P., Theunissen, K., Klerkx, J., 1994, The Palaeoproterozoic Ubendian shear Belt in Tanzania: Geochronology and structure. Journal of African Earth Sciences, 19, 169–184.

Li, J.W., Bi, S.J., Selby, D., Chen, L., Vasconcelos, P., Thiede, D., Zhou, M.F., Zhao, X.F., Li, Z.K., Qiu, H.N., 2012. Giant Mesozoic gold provinces related to the destruction of the North China Craton. Earth and Planetary Sciences Letters, 349−250, 26−27.

Lin, S., Corfu, F., 2002. Structural setting and geochronology of auriferous quartz veins at the High Rock Island gold deposit, northwestern Superior Province, Manitoba, Canada. Economic Geology, 97, 43–57.

Ludwig, K.R., 1998. On the treatment of concordant uranium–lead ages: Geochimica et Cosmochimica Acta, 62, 665–676.

Ludwig, K.A. 2008. User's Manual for Isoplot 3.6, A Geochronological Toolkit for Microsoft Excel. Berkeley Geochronology Center Special Publication, No. 4, 77 p.

Manya, S., Kobayashi, K., Maboko, M.A.H., Nakaruma, E., 2006. Ion microprobe zircon U-Pb dating of the late Archaean metavolcanics and associated granites of the Musoma-Mara greenstone belt, Northeast Tanzania: Implications for the geological evolution of the Tanzania Craton. Journal of African Earth Sciences, 45, 355−366.

Manya, S., 2011. Nd-isotopic mapping of the Archaean-Proterozoic boundary in southwestern Tanzania: Implication for the size of the Archaean Tanzania Craton. Gondwana Research, 20, 325−334.

Manya, S., 2012. SHRIMP zircon U-Pb dating of the mafic and felsic intrusive rocks of the Saza area in the Lupa Goldfields, southwestern Tanzania: Implications for gold mineralization. Natural Science, 4, 724–730.

943 McFarlane, C.R.M., Mavrogenes, J., Lentz, D., King, K., Allibone, A., Holcombe, R., 2011.
944 Geology and intrusion-related affinity of the Morila Gold Mine, southeast Mali. Economic
945 Geology, 106, 727–750.
946
947 Möller, A., Mezger, K., Schenk, V., 1998. Crustal age domains and the evolution of the
948 continental crust in the Mozambique Belt of Tanzania: Combined Sm-Nd, Rb-Sr, and Pb-
949 Pb isotopic evidence. Journal of Petrology, 39, 749–783.
950
951 Morelli, R., Creaser, R.A., Seltmann, R., Stuart, F.M., Selby, D., Graupner, T., 2007. Age and
952 source constraints for the giant Muruntau gold deposit, Uzbekistan, from coupled Re-Os-
953 He isotopes in arsenopyrite. Geology, 35, 795-798.
954
955 Mtoro, M., Maboko, M.A.H., Manya, S., 2009. Geochemistry and geochronology of the bimodal
956 volcanic rocks of the Suguti area in the southern part of the Musoma-Mara Greenstone
957 Belt, Northern Tanzania. Precambrian Research, 174, 241−257.
958
959 Oberthur, T., Vetter, U., Davis, D.W., Amanor, J.A., 1998. Age constraints on gold
960 mineralization and Paleoproterozoic crustal evolution in the Ashanti belt of southern
961 Ghana. Precambrian Research, 89, 129–143.
962
963 Ootes, L., Lentz, D.R., Creaser, R.A., Ketchum, J.W., Falck, H., 2007. Re-Os molybdenite ages
964 from the Archean Yellowknife greenstone belt comparison to U-Pb ages and evidence for
965 metal introduction at similar to 2675 Ma. Economic Geology, 102, 511–518.
966
967 Ootes, L., Morelli, R.M., Creaser, R.A., Lentz, D.R., Falck, H., Davis, W.J., 2011. The timing of
968 Yellowknife gold mineralization a temporal relationship with crustal anatexis. Economic
969 Geology, 106, 713–720.
970
971 Parrish, R.R., 2001. The response of mineral chronometers to metamorphism and deformation in
972 orogenic belts. In: Miller, J.A., Holdsworth, R.E., Buck, I.S., & Hand, M. (Eds.),
973 Continental Reactivation and Reworking. Geological Society, London, Special
974 Publications, 184, 289–301.
975

976 Pettke, T., Diamond, L.W., Villa, I.M., 1999. Mesothermal gold veins and metamorphic
977 devolatilization in the northwestern Alps: The temporal link. Geology, 27, 641–644.
978
979 Phillips, G.N., Powell, R., 2010. Formation of gold deposits; a metamorphic devolatilization
980 model. Journal of Metamorphic Geology, 28, 689–718.
981
982 Pinna, P., Muhongo, S., Mcharo, B., Le Goff, E., Deschamps, Y., 2004. Geology and mineral
983 potential of Tanzania : Digital map at 1:2,000,000 scale. Abstract Volume, 20th Colloquium
984 of African Geology, Orleans, France, June 2−7th.
985
986 Rasmussen, B., Sheppard, S., Fletcher, I.R., 2006. Testing ore deposit models using in situ U-Pb
987 geochronology of hydrothermal monazite: Paleoproterozoic gold mineralization in northern
988 Australia. Geology, 34, 77–80.
989
990 Reddy, S., Collins, A.S., Mruma, A., 2003. Complex high strain deformation in the Usagaran
991 Orogen: Structural setting of Palaeoproterozoic eclogites. Tectonophysics, 375, 101−123.
992
993 Ridley, J.R., Diamond, L.W., 2000. Fluid chemistry of orogenic lode gold deposits and
994 implications for genetic models. SEG Reviews, 13, 141–162
995
996 Roe, A., Essex, M., 2009. Mining in Tanzania – What future can we expect? The Challenge of
997 mineral wealth: Using resource endowments to foster sustainable development.
998 International Council on Mining and Metals (ICMM) Workshop Paper, Tanzania, 54 p.
999
1000 Salier, B.P., Groves, D.I., McNaughton, N.J., Fletcher, I.R., 2005. Geochronological and stable
1001 isotope evidence for widespread orogenic gold mineralization from a deep-seated fluid
1002 source at ca. 2.65 Ga in the Laverton Gold Province, Western Australia. Economic
1003 Geology, 100, 1363–1388.
1004
1005 Sarma, S.D., Fletcher, I.R., Rasmussen, B., McNaughton, N.J., Mohan, M.R., Groves, D.I., 2011.
1006 Archaean gold mineralization synchronous with late cratonization of the Western Dharwar
1007 Craton, India: 2.52 Ga U-Pb ages of hydrothermal monazite and xenotime in gold deposits.
1008 Mineralium Deposita, 46, 273–288.
1009

Şener, A.K., Young, C., Groves, D.I., Krapez, B., Fletcher, I.R., 2005. Major orogenic gold episode associated with Cordilleran-style tectonics related to the assembly of Paleoproterozoic Australia? Geology, 33, 225–228.

Schmitz, M.D., Schoene, B., 2007. Derivation of isotope ratios, errors, and error correlations for U-Pb geochronology using $^{205}Pb$-$^{235}U$($^{233}U$)-spiked isotope dilution thermal ionization mass spectrometric data. Geochemistry, Geophysics, Geosystems, 8, 20 p.

Scholz, C.H., 1988. The brittle-plastic transition and the depth of seismic faulting. Geologische Rundschau, 77, 319–328.

Sibson, R.H., Robert, F., Poulsen, H., 1988. High-angle reverse faults, fluid-pressure cycling, and mesothermal gold-quartz deposits. Geology, 16, 551–555.

Sillitoe, R.H., Thompson, F.H., 1998. Intrusion-related vein gold deposits: types, tectonomagmatic settings and difficulties of distinction from orogenic gold deposits. Resource Geology, 48, 237–250.

Simpson, R., 2012. NI 43-101 mineral resource estimate update for the Saza-Makongolosi gold project, Tanzania. SRK Consulting, www.helioresource.com, 217 p.

Sommer, H., Kroner, A., Hauzenberger, C., Muhongo, S., 2005a. Reworking of Archean Palaeoproterozoic crust in the Mozambique belt of central Tanzania as documented by SHRIMP zircon geochronology. Journal of African Earth Sciences, 43, 447–463.

Sommer, H., Kröner, A., Muhongo, S., and Hauzenberger, C., 2005b. SHRIMP zircon ages for post-Usagaran granitoid and rhyolitic rocks from the Palaeoproterozoic terrain of southwestern Tanzania. South African Journal of Geology, 108, 247−256.

Stacey, J.S., Kramers, J.D., 1975. Approximation of terrestrial lead isotope evolution by a two-stage model. Earth and Planetary Science Letters, 26, 207–221.

1042 Stein, H.J., Morgan, J.W., Scherstén, 2000. Re-Os dating of low-level highly radiogenic (LLHR)
1043 sulfides: The Harnäs gold deposit, southwest Sweden, records continental-scale tectonic
1044 events. Economic Geology, 95, 1657–1671.
1045
1046 Stendal, H., Frei, R., Muhongo, S., Ramussen, T.M., Mnali, S., Petro, F., Temu, E.B., 2004. Gold
1047 potential of the Mpanda Mineral Field, SW Tanzania: Evaluation based on geological, lead
1048 isotopic and aeromagnetic data. Journal of African Earth Sciences, 38, 437–447.
1049
1050 Stern, R.J., 1994. Arc assembly and continental collision in the Neoproterozoic East Africa
1051 Orogen: Implications for the consolidation of Gondwanaland. Annual Reviews of Earth
1052 and Planetary Sciences, 22, 319–351.
1053
1054 Storey, C.D., Jeffries, T.E., Smith, M., 2006. Common lead-corrected laser ablation ICP-MS U-
1055 Pb systematics and geochronology of titanite. Chemical Geology, 227, 37–52.
1056
1057 Tack, L., Wingate, M.T.D., De Waele, B., Meert, J., Belousova, E., Griffin, B., Tahon, A.,
1058 Fernandez-Alonso, M., 2010. The 1375 Ma "Kibran Event" in central Africa: prominent
1059 emplacement of bi-modal volcanism under extensional regime. Precambrian Research,
1060 180, 63–84
1061
1062 Theunissen, K., Klerkx, J., Melnikov, A., Mruma, A., 1996. Mechanisms of inheritance of rift
1063 faulting in the western branch of the east African Rift, Tanzania. Tectonics, 15, 776–790.
1064
1065 Thomas, R.J., Roberts, N.M.W., Jacobs, J., Bushi, A.M., Horstwood, M.S.A., Mruma, A., 2013.
1066 Structural and geochronological constraints on the evolution of the eastern margin of the
1067 Tanzanian Craton in the Mpwapwa area, central Tanzania. Precambrian Research, 224,
1068 671–689
1069
1070 Veilreicher, N.M., Groves, D.I., Snee, L.W., Fletcher, I.R., McNaughton, N.J., 2010. Broad
1071 synchroneity of three gold mineralization styles in the Kalgoorlie Gold Field: SHRIMP,
1072 U-Pb, and $^{40}Ar/^{39}Ar$ Geochronology Evidence. Economic Geology, 105, 187–227.
1073
1074 Van Straaten,H.P., 1984. Gold mineralization in Tanzania — A review. In: Foster R.P., (Ed.),
1075 Gold '82: The Geology, Geochemistry and Genesis of Gold Deposits. Geological Society

of Zimbabwe Special Publication no.1, Proceedings of the Symposium Gold ’82, A.A. Balkema/Rotterdam, 673−685.

Von Quadt, A., Erni, M., Martinek, K., Moll, M., Peytcheva, I., Heinrich, C.A., 2011. Zircon crystallization and the lifetimes of ore-forming magmatic-hydrothermal systems. Geology, 39, 731–734.

Vos, I.M.A., Bierlein, F.P., Standing, J.S., and Davidson, G., 2009. The geology and mineralisation at the Golden Pride gold deposit, Nzega Greenstone Belt, Tanzania. Mineralium Deposita, 44, 751−764.

Walraven, F., Pape, J., Borg, G., 1994. Implications of Pb-isotopic compositions at the Geita gold deposit, Sukumaland Greenstone Belt, Tanzania. Journal of African Earth Sciences, 18, 111−121.

Witt, W.K., Vanderhor, F., 1998. Diversity within a unified model for Archaean gold mineralization in the Yilgarn Craton of Western Australia: An overview of the late-orogenic, structurally-controlled gold deposits. Ore Geology Reviews, 13, 29–64.

Yager, T.R., 2010. The Mineral Industry of Tanzania, in 2010 Minerals Yearbook, US Department of the Interior, U.S. Geological Survey, 39.1−39.7.

**Figure Captions**

Figure 1

Regional geologic map of Tanzania (modified after Pinna et al., 2004; Kabete et al., 2012a). Superterrane abbreviations include (Kabete et al., 2012a, b): East Lake Victoria Superterrane, ELVST; Mwanza-Lake Eyasi Superterrane, MLEST; Lake Nyanza Superterrane, LNST; Moyowosi-Manyoni Superterrane, MMST; Dodoma Basement Superterrane, DBST; Dodoma Schist Superterrane; DSST; Eastern Ubendian-Mtera Superterrane, EUMST; Kalenge-Burigi, KBST, Mbulu-Masai Superterrane, MAST; Kilindi-Handeni Superterrane, KHST; Usagara-Ukaguru Superterrane, UKST; Uluguru-Pare Superterrane; UPST.

Figure 2

Regional geologic map showing the lithotectonic terranes comprising the Palaeoproterozoic Ubendian Belt (modified after Daly, 1988).

Figure 3

Schematic geology map of the Lupa Goldfield (modified after Kimambo, 1984).

Figure 4

Local geology map showing the location of geochronology samples (CL109 and CL0975), mineral systems and artisanal mines. Previously reported U-Pb zircon ages are from Lawley et al. (2013). Eastings and northings are reported as UTM coordinates (WGS84, Zone 36S).

Figure 5

Diagram summarizing previously reported Palaeoproterozoic U-Pb zircon and Re-Os sulphide ages and age ranges, which together with new U-Pb titanite ages, constrain the timing of deformation, magmatism and hydrothermal activity in the Lupa Goldfield. Note the broadly overlapping magmatic and hydrothermal history in the Lupa Goldfield (U-Pb and Re-Os age ranges plotted as horizontal bars; Lawley et al., 2013; Lawley et al., in press-a), whereas individual U-Pb zircon ages (U-Pb zircon ages, without analytical uncertainty, are plotted as vertical bars) show good agreement with three of the temporally distinct hydrothermal events (i.e., ca. 1.95, 1.94, and 1.88 Ga) identified by Re-Os geochronology (weighted average Re-Os ages, without analytical uncertainty, for interpreted hydrothermal events plotted as vertical bars). The ca. 1.88 Ga hydrothermal event is particularly important as it was recorded at all five of the studied gold prospects and also corresponds to the development of D2 auriferous mylonitic shear zones. Note Archaean granites and anomalously younger Mesoproterozoic Re-Os ages are not shown.

Figure 6

(a) Photo of artisanal working along the Kenge shear zone in section view and looking approximately northwest. Fault-fill veins and mylonitic shear zones cut foliated Archaean granite at Kenge; (b) closer photo of fault fill vein and mylonitic shear zone contact at Kenge looking northwest. Note the sharp contact between the mylonite and Archaean granite wall rock (ruler is 15 cm in length); (c) core photo showing complex vein textures that are typical of the fault-fill vein type. Note the laminated vein appearance due to slivers of mylonitized wall rock intercalated

with the fault fill vein; (d–e) core photos of the mineralized zone at Porcupine. Note auriferous quartz veins cutting hydrothermally altered, but non-foliated, Ilunga Syenogranite.

Figure 7

(a) Field photo of foliated Archaean granite sample (CL109); (b) field photo of non-foliated Saza Granodiorite. The Saza Granodiorite is cut by auriferous mylonitic shear zones and quartz veins, but in turns cuts early foliated Archaean granite (not shown). Note overprinting chloritic alteration and en echelon tension gashes; (c) plane polarized light photomicrograph of titanite associated with greenschist facies metamorphic mineral assemblage and tectonic fabric from CL109; (d) plane polarized light photomicrograph of euhedral, and potentially magmatic, titanite crystal from CL0975; (e) stereoscopic photomicrograph showing examples of translucent and fine grained titanite fractions analyzed from CL109; (f) stereoscopic photomicrograph showing examples of fine grained and brown-translucent titanite fractions analyzed from CL0975.

Figure 8

(a–b) Uncorrected (grey ellipses) and corrected [corrected using the Stacey and Kramers (1975) Pb evolution model at 1.9 Ga; S-K; purple ellipses] U-Pb titanite data (purple ellipses) from CL109 and CL0975 on a 2D Terra-Wasserburg plot. Previously reported LA-ICP-MS and ID-TIMS U-Pb zircon ages for CL109 and CL0975, respectively, are also shown for comparison (blue ellipses). The inset figures demonstrate the sensitivity of $^{207}Pb/^{206}Pb$ ages to the assumed isotopic composition of common Pb by varying the Stacey and Kramers (1975) Pb evolution model from 2.5–1.5 Ga. A York Model-1 regression solution of S-K corrected data for CL109 yields an upper intercept U-Pb titanite age of 1921 ± 7 Ma (MSWD = 0.7; n = 7; regression excludes S3 and S4). A York Model-1 regression solution of S-K corrected analyses for CL0975 yields an upper intercept age of 1931 ± 3 Ma (MSWD = 1.1; n =5). The zoomed window in Fig. 6b shows how three of the S-K corrected titanite analyses (purple ellipses) from CL0975 overlap with Concordia and yield a weighted a weighted average $^{207}Pb/^{206}Pb$ age of 1930 ± 3 Ma (MSWD = 0.6; n = 3).

Figure 9

(a–f) Schematic block diagrams showing the geological evolution of the Lupa Goldfield from the Archaean to the Palaeoproterozoic (based on field relationships and U-Pb and Re-Os ages). New U-Pb titanite ages from an Archaean granite suggest that the D1 fabric developed during the Palaeoproterozoic (potentially at ca. 1.92 Ga; Fig. 7e); however the precise timing of D1 remains

unclear since Palaeoproterozoic granites (e.g., Ilunga Syenogranite and Saza Granodiorite) are largely non-foliated, which suggests that the D1 fabric locally pre-dated 1.96 Ga (Fig. 7b) and that younger titanite dates may record Pb-loss. Alternatively, D1 may possess a more complex history than previously recognized and may have developed diachronously during the emplacement of Palaeoproterozoic granites (Fig. 7e). Nevertheless, the New U-Pb titanite ages suggest that ductile deformation predated auriferous mylonites by ≥40 Myr. Note Lupa Goldfield's younger geological history is not shown, but anomalous Mesoproterozoic Re-Os ages and lower intercept U-Pb ages provide evidence for a tectono-thermal history spanning multiple orogenic cycles (Lawley et al., 2013; in press-a). Mineralized structures are also locally offset by cataclasites (not shown) and point to a relatively late and dominantly brittle deformation event (D3) of unknown age.

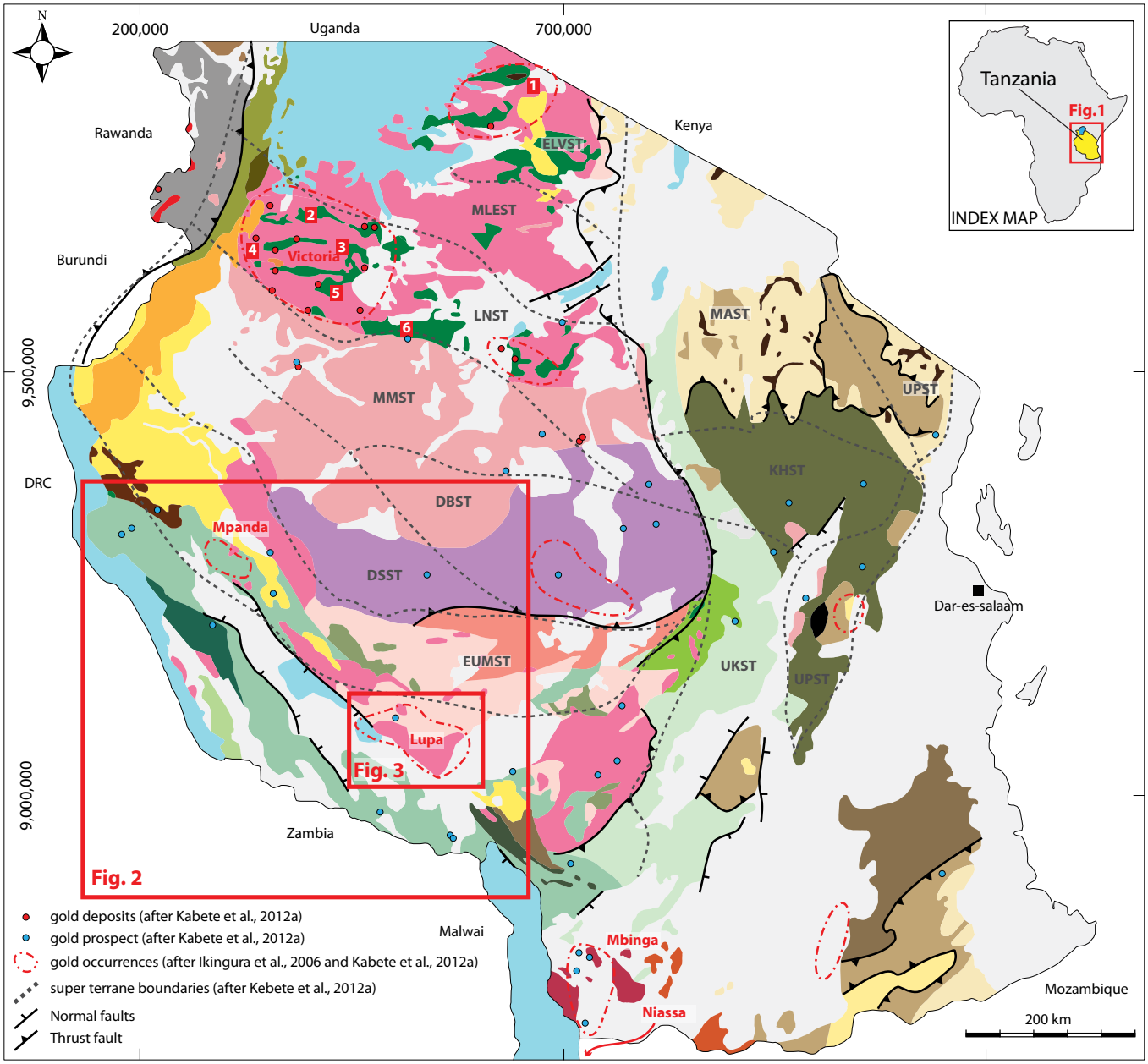


Mesoproterozoic
- Tin granites (~985-950 Ma)
- Mafic rocks
- Meta-sedimentary rocks (ca. 1.37 Ga; previously Bukoban Group)
- Detrital meta-sedimentary rocks
- Shale, sandstone, quartzite (ca. 1.37 Ga)
- Orthogneiss (1.19-0.95 Ga)
- Migmatite and orthogneiss

Palaeoproterozoic (Ubendian-Usagaran Belt)
- Orthogneissic granulite, meta-gabbro, amphibolite, marble, eclogitic lenses (Isimani Group)
- Late orogenic (>1.95 Ga granite, granodiorite)
- Meta-gabbro, anorthosite, ultramafic rocks, Neoproterozoic syenite and granite
- Felsic igneous suites
- Eclogite
- Gneiss, granulite, migmatite, amphibolite, quartzite
- Igneous-sedimentary rocks (ca. 2.61 Ga granulites)

Archaean
- Orthogneiss (TTG), migmatite, granite (Isangan Group, ~3.0-2.85 Ga)
- Orthogneiss (TTG), migmatite, granite (Dodoman Group ~2.90-2.50 Ga)
- Granitoid, migmatite, mafic/ultramafic rock
- Meta-basalt, BIF and phyllite
- Late- to post-orogenic granite/granodiorite

Gold deposits discussed in the text
1. North Mara
2. Geita
3. Bulyanhulu
4. Tulawaka
5. Buzwagi
6. Golden Pride

- Post-Precambrian

Neoproterozoic
- Sedimentary formations
- Volcanic-sedimentary formations
- Marble/quartzite
- Paragneiss (marble, quartzite, schist), orthogneiss (migmatite, amphibolite), granitoid
- Anorthosite complexes (ca. 640 Ma)
- Mafic-felsic granulite, gneiss, migmatite (ca. 640 Ma)
- Neoarchean to Neoproterozoic protoliths re-worked during the tectono-thermal events

# Figure 1

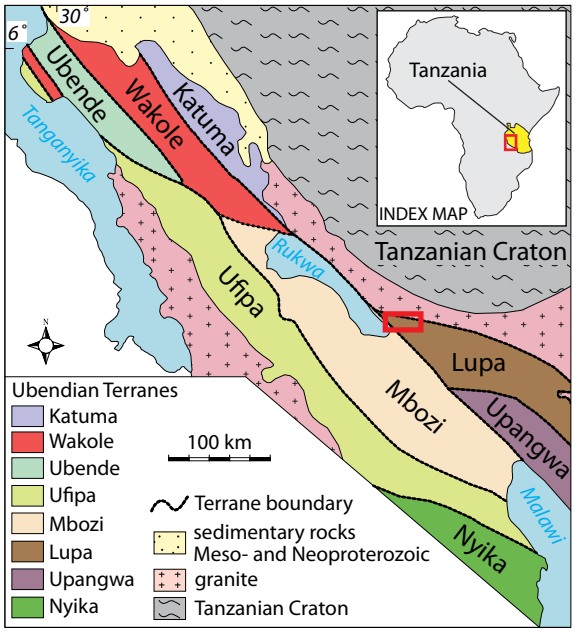
30°
6°
Ubende
Wakole
Katuma
Tanganyika
Rukwa
Ufipa
Mbozi
Lupa
Upangwa
Nyika
Malawi
Tanzania
INDEX MAP
Tanzanian Craton
Ubendian Terranes
Katuma
Wakole
Ubende
Ufipa
Mbozi
Lupa
Upangwa
Nyika
100 km
Terrane boundary
sedimentary rocks
Meso- and Neoproterozoic
granite
Tanzanian Craton

Figure 2

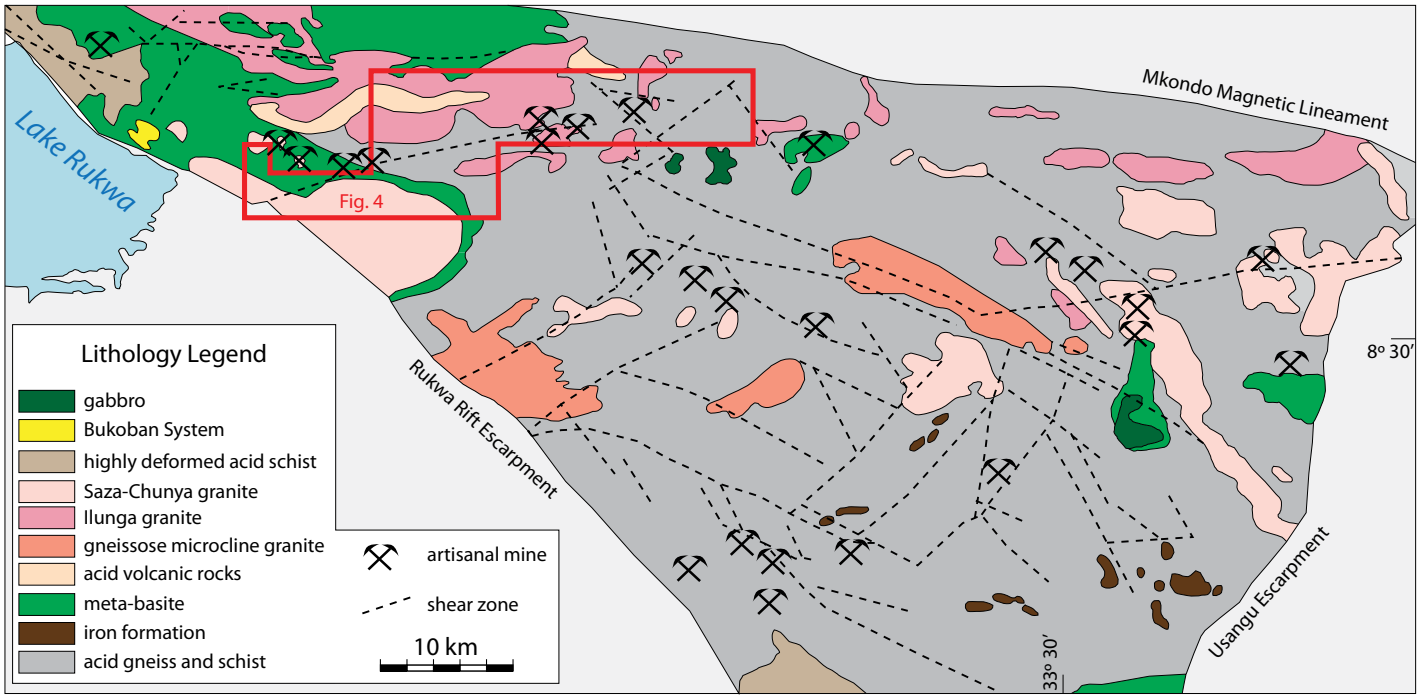
Lake Rukwa
Fig. 4
Mkondo Magnetic Lineament
Rukwa Rift Escarpment
Usangu Escarpment
8° 30'
33° 30'
Lithology Legend
gabbro
Bukoban System
highly deformed acid schist
Saza-Chunya granite
Ilunga granite
gneissose microcline granite
acid volcanic rocks
meta-basite
iron formation
acid gneiss and schist
artisanal mine
shear zone
10 km

Figure 3

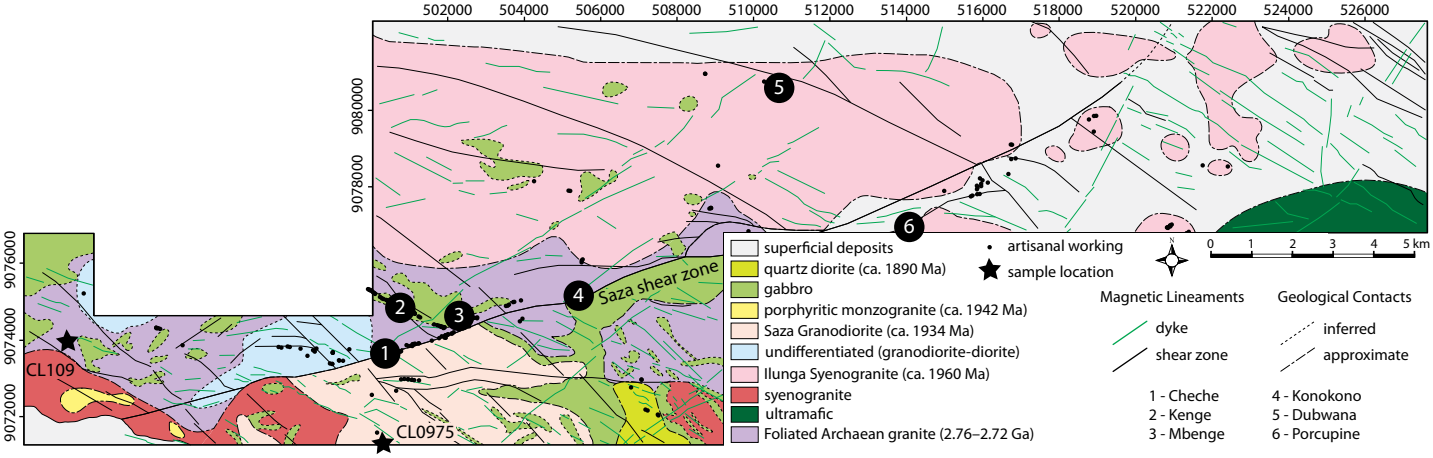
502000
504000
506000
508000
510000
512000
514000
516000
518000
520000
522000
524000
526000
9080000
9078000
9076000
9074000
9072000
CL109
CL0975
Saza shear zone
1
2
3
4
5
6
superficial deposits
quartz diorite (ca. 1890 Ma)
gabbro
porphyritic monzogranite (ca. 1942 Ma)
Saza Granodiorite (ca. 1934 Ma)
undifferentiated (granodiorite-diorite)
Ilunga Syenogranite (ca. 1960 Ma)
syenogranite
ultramafic
Foliated Archaean granite (2.76–2.72 Ga)
artisanal working
sample location
N
0 1 2 3 4 5 km
Magnetic Lineaments
dyke
shear zone
Geological Contacts
inferred
approximate
1 - Cheche
2 - Kenge
3 - Mbenge
4 - Konokono
5 - Dubwana
6 - Porcupine

Figure 4

Palaeoproterozoic Geochronology Summary of the Lupa Goldfield

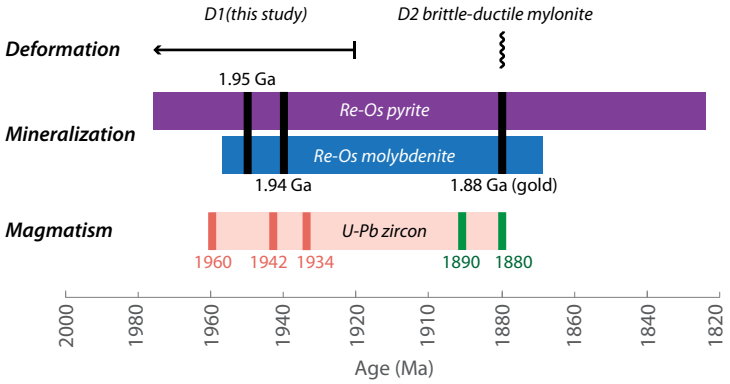


Figure 5

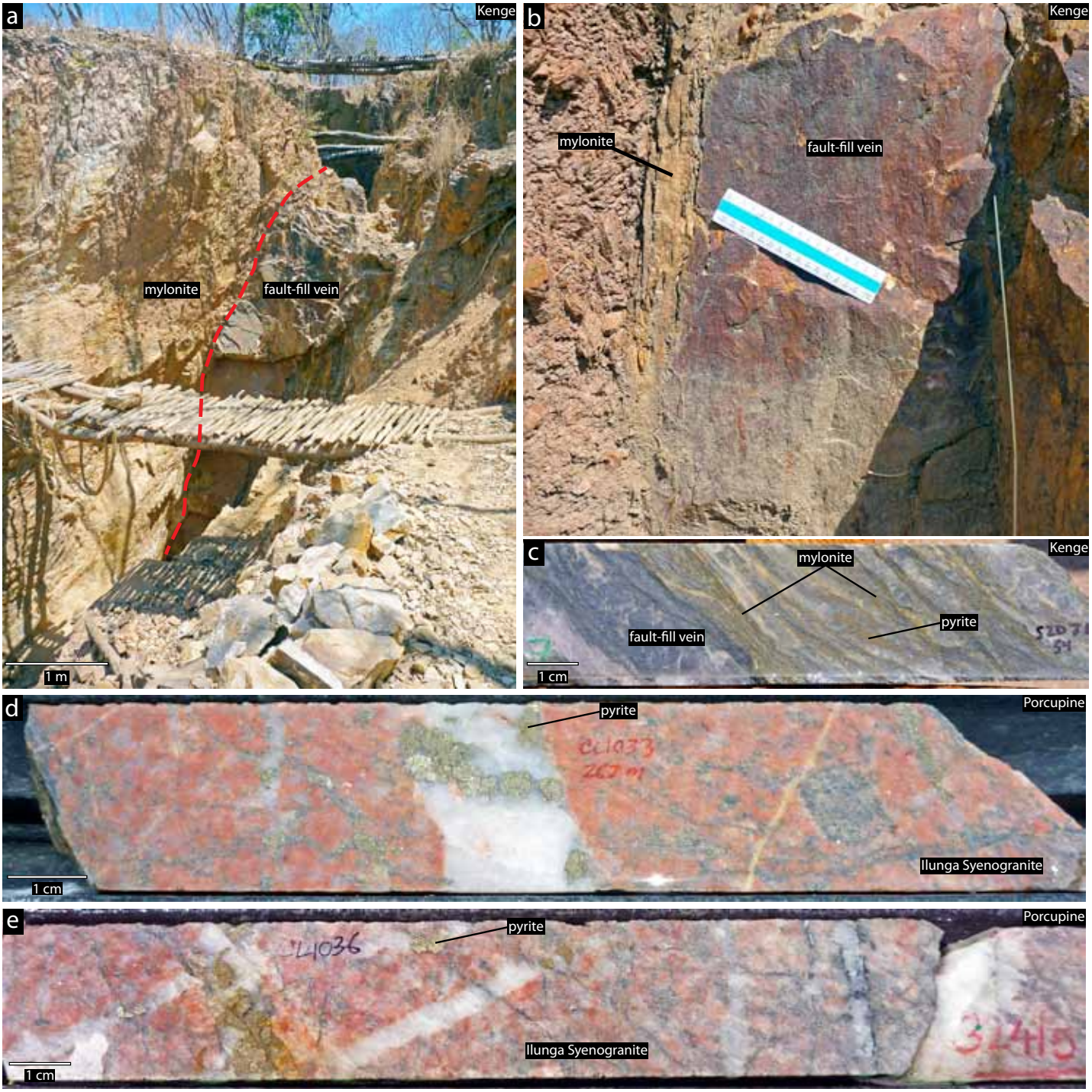
a
Kenge
mylonite
fault-fill vein
1 m
b
Kenge
mylonite
fault-fill vein
c
Kenge
mylonite
pyrite
fault-fill vein
1 cm
d
Porcupine
pyrite
Ilunga Syenogranite
1 cm
e
Porcupine
pyrite
Ilunga Syenogranite
1 cm

Figure 6

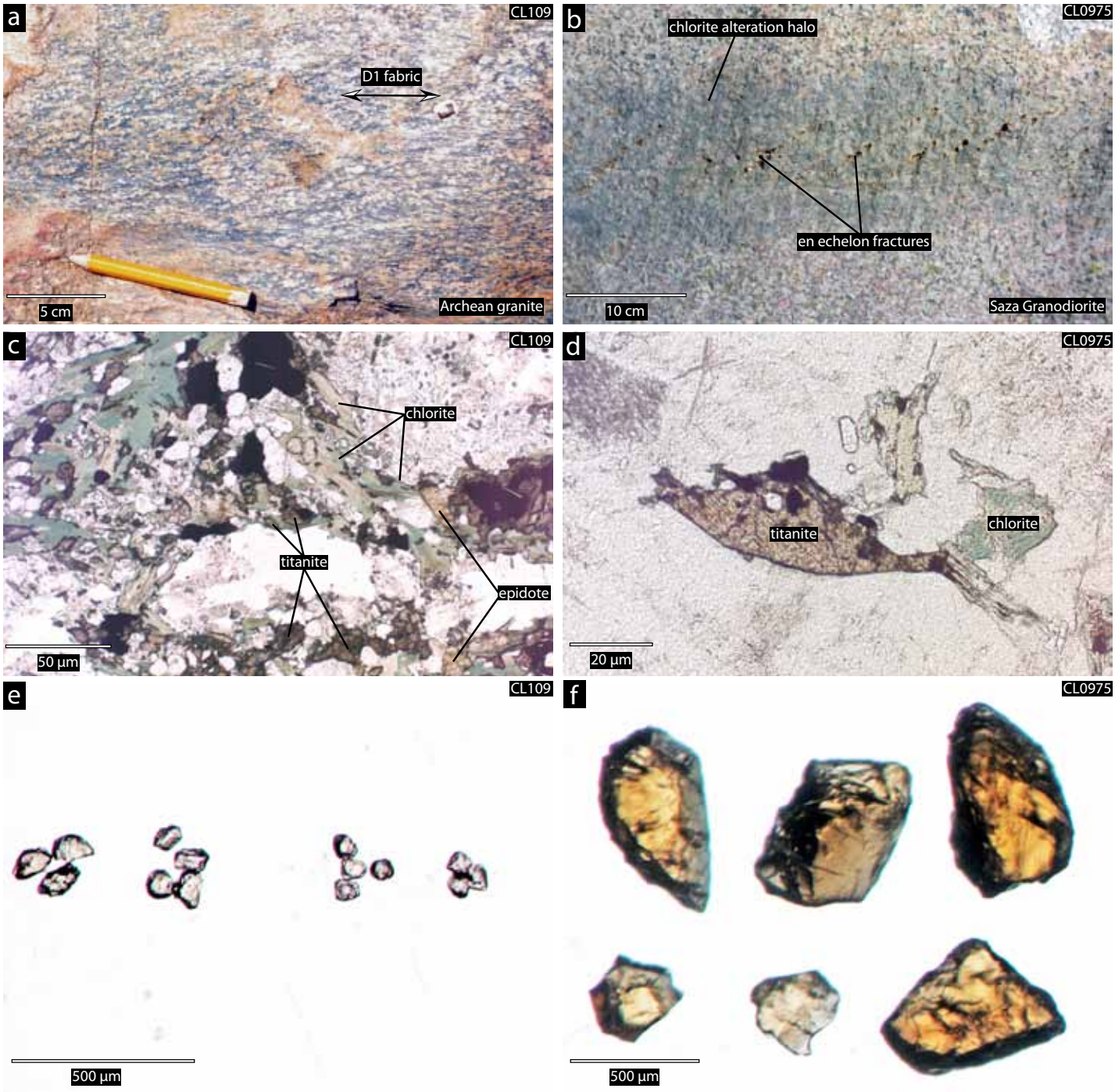
a
CL109
D1 fabric
5 cm
Archean granite
b
CL0975
chlorite alteration halo
en echelon fractures
10 cm
Saza Granodiorite
c
CL109
chlorite
titanite
epidote
50 µm
d
CL0975
titanite
chlorite
20 µm
e
CL109
500 µm
f
CL0975
500 µm

Figure 7

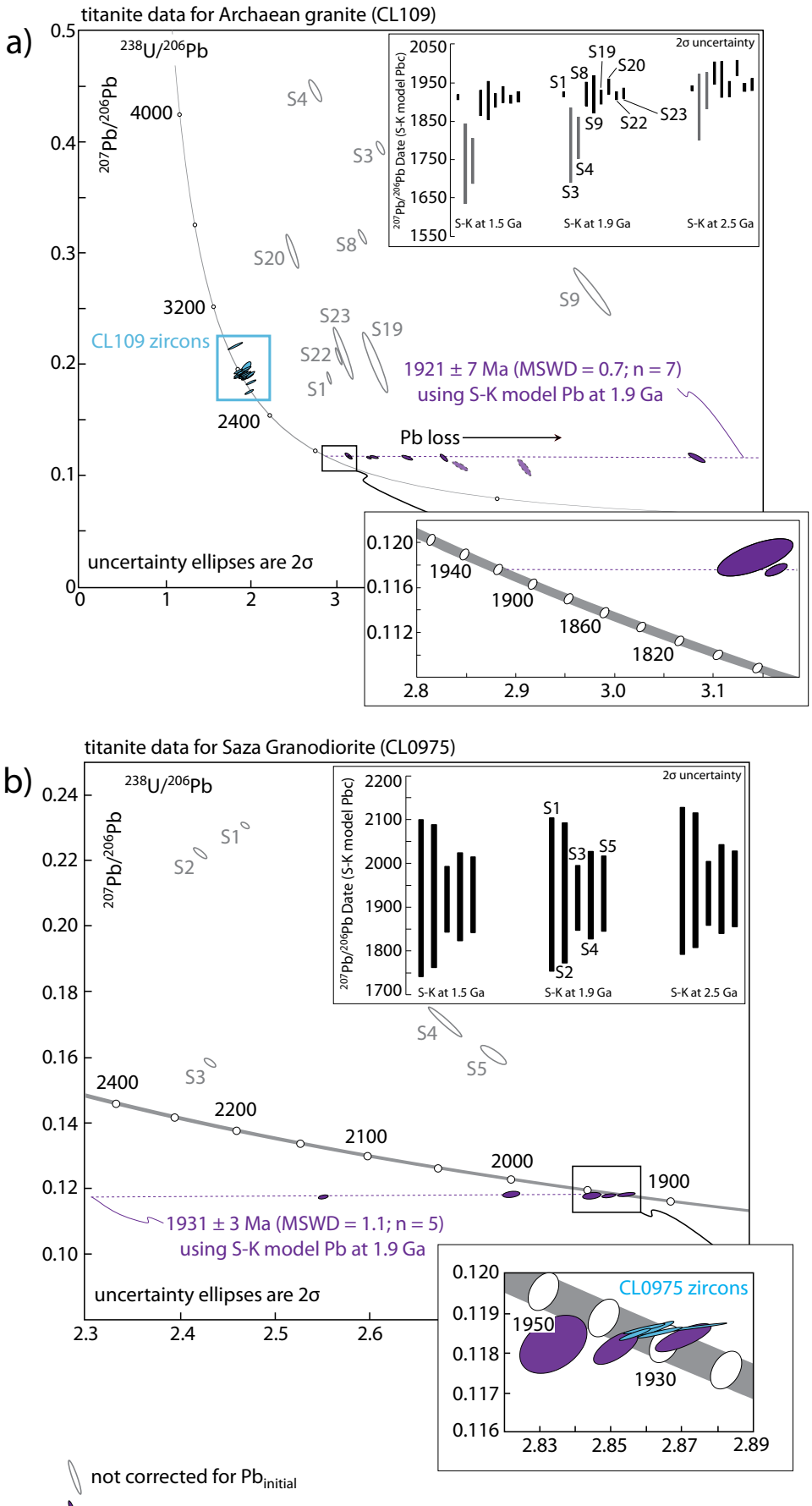
a)
titanite data for Archaean granite (CL109)
$^{238}U/^{206}Pb$
$^{207}Pb/^{206}Pb$
4000
3200
2400
CL109 zircons
1921 ± 7 Ma (MSWD = 0.7; n = 7)
using S-K model Pb at 1.9 Ga
Pb loss
uncertainty ellipses are 2σ
2σ uncertainty
$^{207}Pb/^{206}Pb$ Date (S-K model Pbc)
S-K at 1.5 Ga
S-K at 1.9 Ga
S-K at 2.5 Ga
S1
S3
S4
S8
S9
S19
S20
S22
S23
b)
titanite data for Saza Granodiorite (CL0975)
2400
2200
2100
2000
1900
1931 ± 3 Ma (MSWD = 1.1; n = 5)
using S-K model Pb at 1.9 Ga
CL0975 zircons
1950
1930
not corrected for $Pb_{initial}$
corrected for $Pb_{initial}$ using S-K model Pb at 1.9 Ga
corrected for $Pb_{initial}$ using S-K model Pb at 1.9 Ga, but not used in age regression
zircon analyses (previously reported in Lawley et al., 2013)

Figure 8

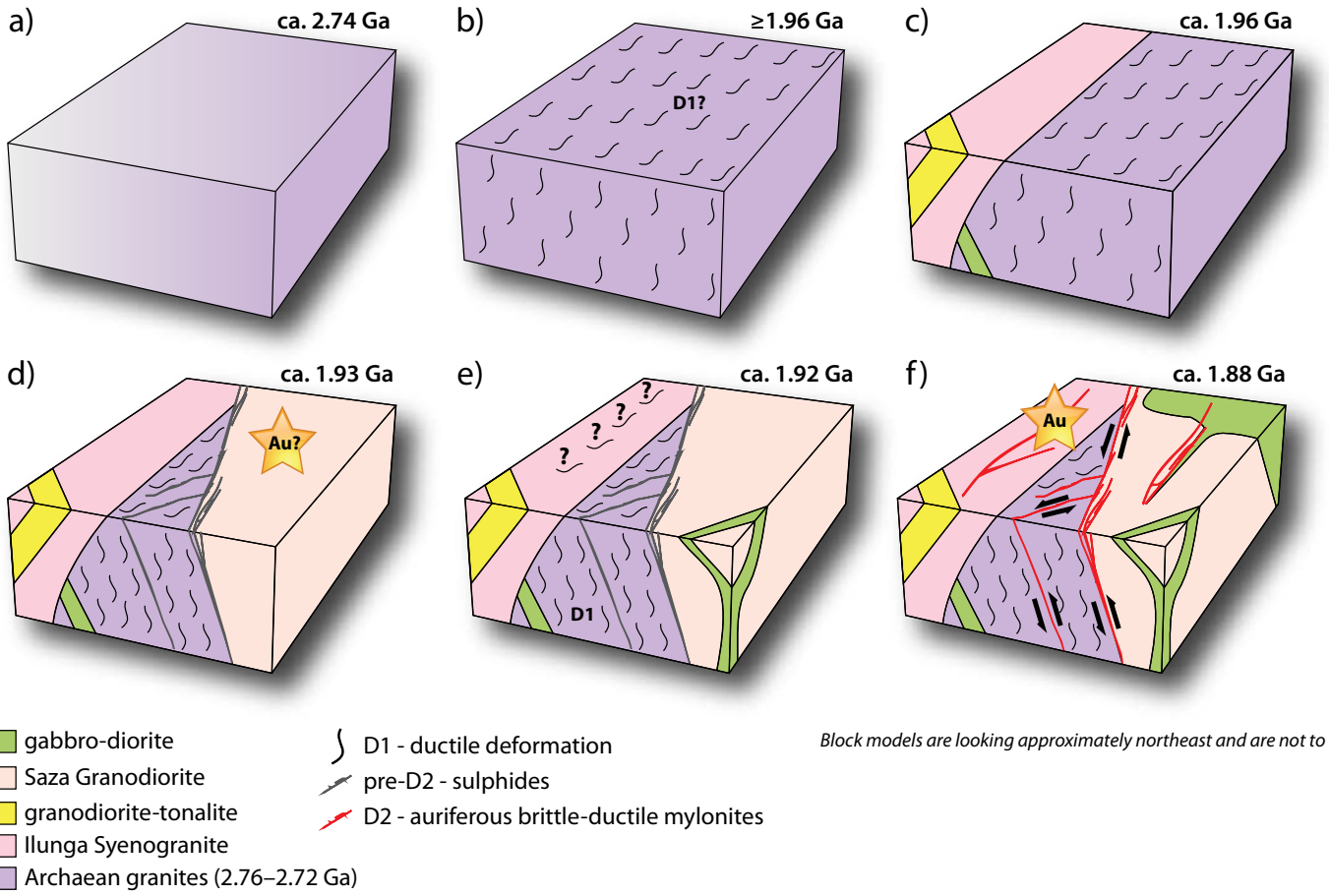


*Block models are looking approximately northeast and are not to scale*

Figure 9

## Table 1. U-Th-Pb isotopic data

| Sample (a) | Th/U (b) | $^{206}Pb^*$ x$10^{-13}$ mol (c) | mol % $^{206}Pb^*$ (c) | Pb*/Pbc (c) | Pbc (pg) (c) | $^{206}Pb/^{204}Pb$ (d) | $^{208}Pb/^{206}Pb$ (e) | $^{207}Pb/^{206}Pb$ (e) | % err (f) | $^{207}Pb/^{235}U$ (e) | % err (f) | $^{206}Pb/^{238}U$ (e) | % err (f) | corr. coef. | $^{207}Pb/^{206}Pb$ (g) | ± (f) | $^{207}Pb/^{235}U$ (g) | ± (f) | $^{206}Pb/^{238}U$ (g) | ± (f) | $^{238}U/^{206}Pb$ (h) | % err (f) | $^{207}Pb/^{206}Pb$ (h) | % err (f) | $^{204}Pb/^{206}Pb$ (h) | % err (f) | corr. coef. 8/6-7/6 | corr. coef. 8/6-4/6 | corr. coef. 7/6-4/6 | $^{238}U/^{204}Pb$ (h) | % err (f) | $^{206}Pb/^{204}Pb$ (h) | % err (f) | corr. coef. 8/4-6/4 | $^{235}U/^{204}Pb$ (h) | % err (f) | $^{207}Pb/^{204}Pb$ (h) | % err (f) | corr. coef. 5/4-7/4 |
|---|---|---|---|---|---|---|---|---|---|---|---|---|---|---|---|---|---|---|---|---|---|---|---|---|---|---|---|---|---|---|---|---|---|---|---|---|---|---|
| **CL109** | | | | | | | | | | | | | | | | | | | | | | | | | | | | | | | | | | | | | | |
| s1 | 8.685 | 1.8765 | 91% | 9 | 17 | 172 | 2.63713 | 0.11757 | 0.37158 | 5.12124 | 0.50024 | 0.31607 | 0.28828 | 0.677 | 1919 | 7 | 1840 | 4 | 1770 | 4 | 2.90842 | 0.63551 | 0.18816 | 2.11335 | 0.00525 | 5.54664 | -0.94304 | -0.93364 | 0.99647 | 553.460993 | 6.144194 | 190.296410 | 5.546638 | 0.999313 | 4.015883 | 6.144194 | 35.807065 | 3.445327 | 0.997181 |
| s3 | 5.561 | 0.9342 | 66% | 1 | 42 | 46 | 2.05308 | 0.10859 | 5.43178 | 2.87496 | 5.92031 | 0.19210 | 1.16198 | 0.501 | 1775 | 99 | 1375 | 45 | 1133 | 12 | 3.51867 | 1.01569 | 0.39489 | 1.10399 | 0.02109 | 1.74569 | -0.81246 | -0.67796 | 0.72454 | 166.806967 | 2.546213 | 47.406231 | 1.745688 | 0.956041 | 1.210342 | 2.546213 | 18.720344 | 1.213880 | 0.628353 |
| s4 | 8.675 | 0.4079 | 60% | 1 | 25 | 39 | 3.00279 | 0.10955 | 3.04999 | 3.38886 | 3.34017 | 0.22445 | 1.52124 | 0.410 | 1791 | 56 | 1502 | 26 | 1305 | 18 | 2.75546 | 2.09995 | 0.44626 | 1.69109 | 0.02484 | 2.19780 | -0.87946 | -0.86615 | 0.98221 | 110.950266 | 4.151525 | 40.265570 | 2.197802 | 0.967517 | 0.805049 | 4.151525 | 17.968907 | 0.623712 | 0.793318 |
| s8 | 10.142 | 1.0647 | 76% | 3 | 30 | 65 | 3.56932 | 0.11734 | 1.77519 | 3.78833 | 1.97265 | 0.23427 | 0.67383 | 0.449 | 1916 | 32 | 1590 | 16 | 1357 | 8 | 3.30306 | 0.96507 | 0.31520 | 1.52549 | 0.01472 | 2.45117 | -0.91463 | -0.87908 | 0.95269 | 224.332673 | 3.331458 | 67.916560 | 2.451167 | 0.990420 | 1.627746 | 3.331458 | 21.407120 | 1.100327 | 0.867201 |
| s9 | 6.544 | 0.3543 | 78% | 3 | 9 | 75 | 2.89817 | 0.11743 | 2.74106 | 2.23765 | 3.14245 | 0.13826 | 1.03516 | 0.528 | 1917 | 49 | 1193 | 22 | 835 | 8 | 5.99911 | 2.93770 | 0.26660 | 6.28610 | 0.01110 | 11.09868 | -0.97046 | -0.96419 | 0.99294 | 540.393150 | 13.952954 | 90.078859 | 11.098684 | 0.998440 | 3.921064 | 13.952954 | 24.014967 | 4.913830 | 0.983361 |
| s19 | 6.808 | 0.3295 | 85% | 4 | 5 | 107 | 2.27226 | 0.11711 | 1.02463 | 4.21270 | 1.77968 | 0.26101 | 1.24656 | 0.827 | 1912 | 18 | 1676 | 15 | 1495 | 17 | 3.45787 | 3.49886 | 0.20239 | 10.74043 | 0.00634 | 25.09789 | -0.95339 | -0.95246 | 0.99918 | 545.070753 | 28.450395 | 157.631917 | 25.097887 | 0.999298 | 3.955004 | 28.450395 | 31.902666 | 14.372904 | 0.998682 |
| s20 | 4.450 | 0.4556 | 76% | 2 | 13 | 65 | 1.35284 | 0.11869 | 1.16054 | 5.20495 | 1.56029 | 0.31821 | 0.99986 | 0.669 | 1936 | 21 | 1853 | 13 | 1781 | 16 | 2.48128 | 2.24673 | 0.30248 | 3.84972 | 0.01370 | 6.22461 | -0.93974 | -0.93702 | 0.99762 | 181.144783 | 8.366722 | 73.004701 | 6.224608 | 0.995592 | 1.314377 | 8.366722 | 22.082102 | 2.398797 | 0.987342 |
| s22 | 8.289 | 1.1981 | 88% | 6 | 15 | 131 | 2.60140 | 0.11730 | 0.61527 | 4.78081 | 0.77432 | 0.29572 | 0.39822 | 0.616 | 1915 | 11 | 1782 | 7 | 1670 | 6 | 3.02946 | 0.95581 | 0.20839 | 2.82371 | 0.00678 | 6.36678 | -0.95466 | -0.94810 | 0.99587 | 446.960561 | 7.279330 | 147.537871 | 6.366777 | 0.999128 | 3.243122 | 7.279330 | 30.745556 | 3.563952 | 0.995452 |
| s23 | 11.093 | 0.3767 | 84% | 6 | 6 | 105 | 3.51968 | 0.11774 | 0.76732 | 4.71338 | 1.43760 | 0.29046 | 1.04548 | 0.855 | 1922 | 14 | 1770 | 12 | 1644 | 15 | 3.07716 | 3.01549 | 0.21060 | 8.82788 | 0.00691 | 19.70896 | -0.95833 | -0.95740 | 0.99936 | 445.127104 | 22.612749 | 144.655189 | 19.708961 | 0.999258 | 3.229818 | 22.612749 | 30.464599 | 10.891381 | 0.998668 |
| **CL0975** | | | | | | | | | | | | | | | | | | | | | | | | | | | | | | | | | | | | | | |
| s1 | 7.101 | 12.6005 | 87% | 5 | 170 | 118 | 2.04070 | 0.11825 | 0.50689 | 5.75101 | 0.54341 | 0.35288 | 0.27228 | 0.380 | 1929 | 9 | 1939 | 5 | 1948 | 5 | 2.46803 | 0.14137 | 0.23103 | 0.24519 | 0.00840 | 0.49173 | -0.73746 | -0.36875 | 0.75343 | 293.758217 | 0.559511 | 119.025226 | 0.491732 | 0.972030 | 2.131494 | 0.559511 | 27.498842 | 0.346756 | 0.778471 |
| s2 | 7.024 | 5.5666 | 88% | 5 | 70 | 126 | 1.98811 | 0.11854 | 0.46212 | 5.94430 | 0.50466 | 0.36387 | 0.25145 | 0.411 | 1934 | 8 | 1968 | 4 | 2000 | 4 | 2.42092 | 0.21977 | 0.22257 | 0.55365 | 0.00775 | 1.16458 | -0.91991 | -0.81574 | 0.95534 | 312.275906 | 1.349856 | 128.990334 | 1.164580 | 0.995556 | 2.265857 | 1.349856 | 28.709537 | 0.656374 | 0.944823 |
| s3 | 6.545 | 8.6624 | 95% | 13 | 40 | 315 | 1.77382 | 0.11777 | 0.21445 | 6.36479 | 0.29163 | 0.39214 | 0.14130 | 0.716 | 1922 | 4 | 2027 | 3 | 2133 | 3 | 2.43100 | 0.17231 | 0.15861 | 0.59326 | 0.00304 | 2.25488 | -0.83437 | -0.74161 | 0.97755 | 799.518730 | 2.385468 | 328.884369 | 2.254876 | 0.998825 | 5.801265 | 2.385468 | 52.164448 | 1.679597 | 0.993264 |
| s4 | 7.634 | 2.3294 | 93% | 10 | 15 | 226 | 2.20028 | 0.11816 | 0.28857 | 5.71131 | 0.37949 | 0.35072 | 0.17821 | 0.684 | 1928 | 5 | 1933 | 3 | 1938 | 3 | 2.67886 | 0.50225 | 0.17101 | 1.96415 | 0.00394 | 6.25903 | -0.98383 | -0.97258 | 0.99661 | 680.509624 | 6.748516 | 254.029522 | 6.259025 | 0.999850 | 4.937741 | 6.748516 | 43.441625 | 4.304555 | 0.998652 |
| s5 | 6.950 | 3.5224 | 94% | 13 | 18 | 285 | 2.01251 | 0.11841 | 0.24778 | 5.68564 | 0.37252 | 0.34839 | 0.22256 | 0.765 | 1932 | 4 | 1929 | 3 | 1927 | 4 | 2.73024 | 0.38223 | 0.16105 | 1.41795 | 0.00318 | 5.28003 | -0.87134 | -0.85159 | 0.99345 | 859.439228 | 5.609118 | 314.785585 | 5.280033 | 0.999362 | 6.236045 | 5.609118 | 50.696522 | 3.874763 | 0.997856 |

(a) z1, z2 etc. are labels for fractions composed of single zircon grains or fragments; all fractions annealed and chemically abraded after Mattinson (2005).

(b) Model Th/U ratio calculated from radiogenic $^{208}Pb/^{206}Pb$ ratio and $^{207}Pb/^{235}U$ age.

(c) Pb* and Pbc represent radiogenic and common Pb, respectively; mol % $^{206}Pb^*$ with respect to radiogenic, blank and initial common Pb.

(d) Measured ratio corrected for spike and fractionation only.
Daly analyses, based on analysis of NBS-981 and NBS-982.

(e) Corrected for fractionation, spike, and common Pb; up to 1 pg of common Pb was assumed to be procedural blank: $^{206}Pb/^{204}Pb = 18.60 \pm 0.80\%$; $^{207}Pb/^{204}Pb = 15.69 \pm 0.32\%$; $^{208}Pb/^{204}Pb = 38.51 \pm 0.74\%$ (all uncertainties 1-sigma). Excess over blank was assigned to initial common Pb.

(f) Errors are 2-sigma, propagated using the algorithms of Schmitz and Schoene (2007) and Crowley et al. (2007).

(g) Calculations are based on the decay constants of Jaffey et al. (1971). $^{206}Pb/^{238}U$ and $^{207}Pb/^{206}Pb$ ages corrected for initial disequilibrium in $^{230}Th/^{238}U$ using Th/U [magma] = 3.

(h) Corrected for fractionation, spike, and blank Pb only.

**Table 3. Summary of geologic characteristics at Tanzanian gold deposits and goldfields**

| Goldfield/Region | Significant Deposits | Host Rock | Host Rock Age (Ga) | Ore Controls | Hydrothermal Alteration Mineral Assemblage | Metamorphic facies | Metals | Sulphide Assemblage | Gold (Ga) | Method | Source |
|---|---|---|---|---|---|---|---|---|---|---|---|
| **Goldfields within the Tanzanian Craton** | | | | | | | | | | | |
| Lake Victoria | North Mara | sedimentary and volcanic rocks, granodiorite, tonalite, porphyritic andesite/dacite, gabbro | 2.76−2.65 | shear and quartz vein hosted; lithologic contact control | Ser ± Chl ± Carb ± Sil ± Pot ± Sod | greenschist | Au ± Cu | Py ± Cpy ± Po | 2.69−2.64 | constrained by U-Pb zircon dating of magmatism and/or deformation | Manya et al., 2006; Kabete, 2008; Kazimoto, 2008; Mtoro et al., 2009; Ikingura et al., 2009 |
| | Geita | BIF, felsic-mafic volcanic and sedimentary rocks | 2.84−2.64 | BIF, fault and quartz vein control | Carb ± Sil ± ? | amphibolite to greenschist | Au | Py ± Po ± Cpy ± Asp | ≤2.644 | U-Pb zircon dating of pre-gold lamprophyre dike | Walraven and Borg, 1994; Borg and Krough, 1999; Kabete et al., 2012a |
| | Bulyanhulu | sedimentary (including graphitic argillite), and felsic-mafic volcanic rocks | 2.84−2.64 | shear (breccia) and quartz vein hosted; lithologic contact control | Ser ± Chl ± Carb ± Sil | greenschist | Au ± Cu ± Pb | Py ± Po ± Asp ± Cpy ± Gal | 2.69−2.63 | constrained by U-Pb zircon dating of magmatism and/or deformation | Chamberlain, 2003; Kabete et al., 2012a |
| | Tulawaka | mafic-felsic volcanic and sedimentary rocks, granite, aplite dikes | 2.84−2.64 | shear and quartz vein hosted; lithologic contact control | ? | amphibolite to greenschist | Au | ? | 2.69−2.63 | constrained by U-Pb zircon dating of magmatism and/or deformation | Cloutier et al., 2005; Kabete et al., 2012a |
| | Buzwagi | granite and lesser mafic volcanic rocks | 2.84−2.64 | shear and quartz vein hosted | Ser ± Sil ± ? | greenschist | Au ± Cu | Py ± Cpy | 2.69−2.63 | constrained by U-Pb zircon dating of magmatism and/or deformation | Ikingura et al., 2009 |
| | Golden Pride | sedimentary (predominately sandstone/siltstone) rocks, BIF, dacitic intrusions | 2.7 to <2.65 | shear and quartz vein hosted; lithologic control | Ser ± Chl ± Carb ± Biot ± Cltd | greenschist | Au | Po + Asp + Py + Cpy ± Gal ± Sph ± Stb ± Tel ± Co-Ni-Bi sulphides | ca. 2.68 | U-Pb dating of co-genetic magmatic phases | Vos et al., 2009; Kwelwa et al., 2012a |
| Central Tanzania | mainly artisanal workings | amphibolite, granitic gneisses; mafic volcanic and sedimentary rocks (including BIF) | 2.82−2.66 | shear and quartz vein hosted | Sil ± Pot ± Chl | amphibolite to greenschist | Au | Py ± ? | 2.70−2.66 | constrained by U-Pb zircon dating of magmatism and/or deformation | Kabete et al., 2012a |
| **Goldfields at cratonic margins** | | | | | | | | | | | |
| Lupa | Kenge<br>Mbenge<br>Porcupine | granite, granodiorite, gabbro | 2.76−1.88 | shear and quartz vein hosted; lithologic contact control | Ser ± Chl ± Carb ± Sil | greenschist | Au | Py ± Cpy ± Gal ± Mo ± Sph | ca. 1.88 | Re-Os pyrite | Lawley et al., in press |
| Mpanda | mainly artisanal workings | orthogneisses, metapelites, metabasites, gabbro | 2.65−1.93 | shear and quartz vein hosted | Ser ± Chl ± Carb | granulite to greenschist | Pb ± Cu ± Au ± Ag | Gal + Cpy + Py | ca. 1.2?<br>ca. 0.72? | U-Pb monazite<br>Pb-Pb galena | Kuehn et al., 1990; Stendal et al., 2004; Kazimoto and Schenk, 2013 |
| Niassa | mainly artisanal workings | sedimentary rocks, gabbro | ca. 0.714 | shear and quartz vein hosted | Chl ± Carb ± Grun ± Ser | greenschist | Au | Py ± Cpy ± Mar ± Po ± Sph | ca. 0.483 | Re-Os pyrite | Bjerkgard et al., 2009 |
| Burundi | mainly artisanal workings | volcanic and sedimentary rocks, granite | 1.78−1.37 | shear, quartz vein, and breccia hosted | Ser ± Tour ± Oxides | greenschist | Au ± Sn ± W ± Bi | Py ± Asp ± Cpy ± Bi-sulphides ± oxides (cassiterite ± hematite) | ca. 1.0−0.9<br>ca. 0.64 | Rb-Sr whole rock, muscovite, and tourmaline | Brinckmann et al., 1994; Fernandez-Alonso et al., 2012 |

List of abbreviations used. Hydrothermal alteration mineral assemblage: Ser = sercitie, Chl = chlorite, Carb = carbonate mienrals, Sil = silica flooding, Grun = grunerite, Pot = potassic, Sod = sodic, Cltd = chloritoid, Tour = tourmaline, Oxides = oxide minerals. Sulphide Assemblage: Py = pyrite, Cpy = chalcopyrite, Po = pyrrhotite, Asp = arsenopyrite, Gal = galena, Sph = sphalerite, Stb = stibnite, Tel = telurides, Mo = molybdenite, Mar = marcasite.

**Table. 1 - Geochronology Summary**

| Sample ID | Sample type | Analysis method | | Interpreted age (Ma) | Analytical Uncertainty at 2σ (Ma) | Age determination method |
|---|---|---|---|---|---|---|
| CL0975 | Saza Granodiorite | U-Pb zircon[1] | ID-TIMS | 1934.5 | 1.0 | weighted average $^{207}Pb/^{206}Pb$ concordant zircon age |
| CL0972 | Ilunga Syenogranite | U-Pb zircon[1] | ID-TIMS | 1959.6 | 1.1 | weighted average $^{207}Pb/^{206}Pb$ concordant zircon age |
| CL0911 | granodiorite dike cutting foliated granite (CL098) | U-Pb zircon[1] | ID-TIMS | 1958.5 | 1.3 | weighted average $^{207}Pb/^{206}Pb$ concordant zircon age |
| CL098 | foliated granite | U-Pb zircon[1] | LA-MC-ICP-MS | 2723 | 10 | weighted average $^{207}Pb/^{206}Pb$ concordant zircon age |
| CL1020 | foliated granite | U-Pb zircon[1] | LA-MC-ICP-MS | 2739 | 10 | weighted average $^{207}Pb/^{206}Pb$ concordant zircon age |
| CL109 | foliated granite | U-Pb zircon[1] | LA-MC-ICP-MS | 2758 | 9 | weighted average $^{207}Pb/^{206}Pb$ concordant zircon age |
| CL1019 | porphyritic monzogranite | U-Pb zircon[1] | LA-MC-ICP-MS | 1942 | 14 | weighted average $^{207}Pb/^{206}Pb$ concordant zircon age |
| CL1021 | quartz diorite | U-Pb zircon[1] | LA-MC-ICP-MS | 1891 | 17 | upper intercept Concordia age |
| CL1022 | gabbroic dike cutting foliated granite (CL109) | U-Pb zircon[1] | LA-MC-ICP-MS | 1880 | 17 | upper intercept Concordia age |
| multiple samples | ultrafine molybdenite from Kenge | Re-Os molybdenite[2] | N-TIMS | 1953 | 6 | weighted average Re-Os model age |
| multiple samples | molybdenite from Kenge | Re-Os molybdenite[2] | N-TIMS | 1937 | 4 | weighted average Re-Os model age |
| multiple samples | pyrite from mylonitic shear zone at Kenge and Mbenge | Re-Os pyrite[2] | N-TIMS | 1876 | 10 | weighted average Re-Os model age |
| multiple samples | pyrite and chalopyrite from quartz veins at Kenge | Re-Os pyrite chalcopyrite[2] | N-TIMS | 1953 | 37 | weighted average Re-Os model age |
| multiple samples | | | | 1871 | 12 | |
| multiple samples | pyrite and chalcopyrite from quartz veins at Konokono | Re-Os pyrite chalcopyrite[2] | N-TIMS | 1885 | 9 | weighted average Re-Os model age |
| multiple samples | | | | 1371 | 160 | |
| multiple samples | | | | 975 | 6 | |
| multiple samples | ultrafine molybdenite from Porcupine | Re-Os molybdenite[2] | N-TIMS | 1886 | 6 | weighted average Re-Os model age |
| multiple samples | molybdenite from Porcupine | Re-Os molybdenite[2] | N-TIMS | 1873 | 5 | weighted average Re-Os model age |
| multiple samples | | | | 1894 | 45 | |
| multiple samples | pyrite from Porcupine | Re-Os pyrite[2] | N-TIMS | 1057 | 56 | weighted average Re-Os model age |
| multiple samples | | | | 922 | 190 | |
| multiple samples | pyrite from Dubwana | Re-Os pyrite[2] | N-TIMS | 1910 | 38 | individual Re-Os model ages |
| multiple samples | | | | 1900 | 38 | |
| CL109 | foliated granite | U-Pb titanite[3] | ID-TIMS | 1921 | 7 | upper intercept Concordia age |
| CL0975 | Saza Granodiorite | U-Pb titanite[3] | ID-TIMS | 1930 | 3 | weighted average $^{207}Pb/^{206}Pb$ concordant titanite age |

[1]Data takern from Lawley et al., 2013
[2]Data taken from Lawley et al., in press-a
[3]Data from this study